



<http://www.spring8.or.jp>

<http://xfel.riken.jp>

Registered Institution for Facilities Use Promotion
Japan Synchrotron Radiation Research Institute

1-1-1 KOUTO, SAYO-CHO, SAYO-GUN, HYOGO 679-5198, JAPAN

Information and Outreach Section

Tel:+81-791-58-2785

Fax:+81-791-58-2786

User Administration Division

Tel:+81-791-58-0961

Fax:+81-791-58-0965

SPRING-8

Japan Synchrotron Radiation Research Institute



Introduction

Synchrotron radiation (SR) is extremely powerful light which is used for studying the structure of matter at the atomic and electronic levels and in various physical and chemical processes in a number of research fields ranging from materials science to life science.

SPring-8, which is one of the largest third-generation synchrotron radiation facilities in the world, provides the most powerful synchrotron radiation currently available. Construction of SPring-8 was started in 1991 and the facility was opened in October 1997.

At SPring-8, many scientists from around the world are making efforts to unlock the secrets of nature using synchrotron radiation as the key.

SPring-8 Storage Ring Parameters

Electron energy	8 GeV	Characteristic photon energy	28.9 keV
Current	100 mA	Number of insertion devices	Max. 38
Circumference	1,436 m	Number of beamlines	Max. 62

Synchrotron Radiation

What is Synchrotron Radiation?

Synchrotron radiation (SR) is emitted from an electron traveling at almost the speed of light when its path is bent by a magnetic field. As it was first observed in a synchrotron in 1947, it was named "synchrotron radiation".

General Features of Synchrotron Radiation

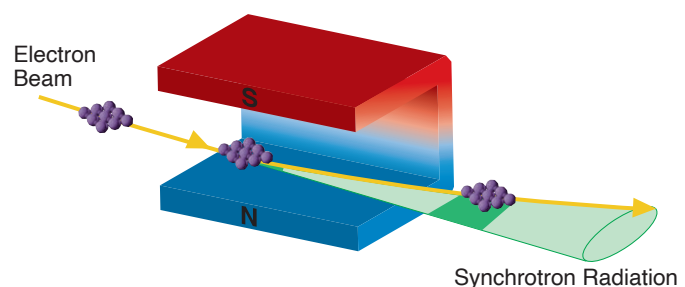
- Ultra-bright
- Highly directional
- Spectrally continuous (BM/W) or quasi-monochromatic (U)
- Linearly or circularly polarized
- Pulsed with controlled intervals
- Temporally and spatially stable

BM: Bending Magnet
W : Wiggler
U : Undulator

Generation of Synchrotron Radiation

Synchrotron radiation is emitted at a bending magnet or at an insertion device. The insertion device is comprised of rows of magnets with alternating polarity and is installed in a straight section of the electron orbit. Corresponding to the weak and strong magnetic field, there are two types of insertion devices: an undulator and a wiggler.

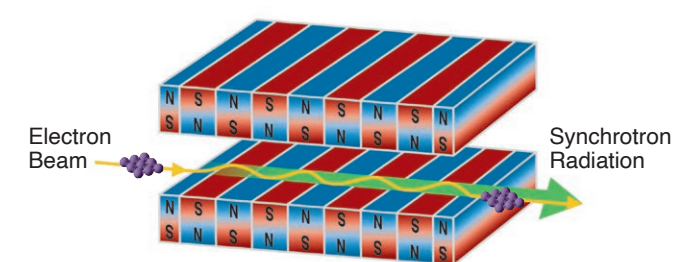
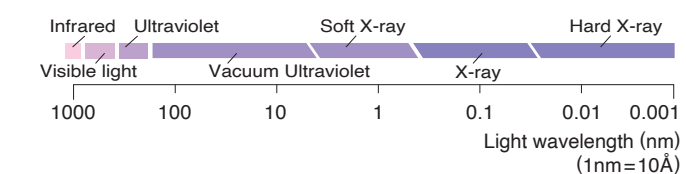
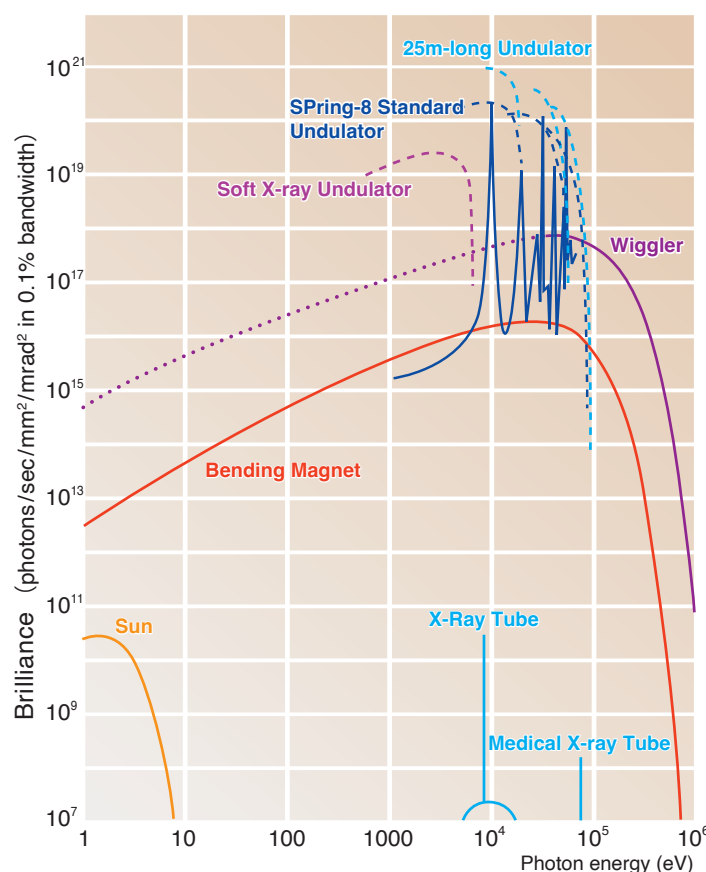
- Bending Magnet** ● Stored electrons run on a circular orbit and emit synchrotron radiation with a continuous spectrum when they encounter the bending magnet.
- Undulator** ● The electron beam undulates with a small deviation angle. As a result, ultra-bright and quasi-monochromatic light is obtained by the interference effect.
- Wiggler** ● The electron beam wiggles with a large deviation angle. As a result, bright and spectrally continuous light with short wavelengths is obtained.



▲ Synchrotron radiation produced at a bending magnet

Synchrotron Radiation Spectrum of SPring-8

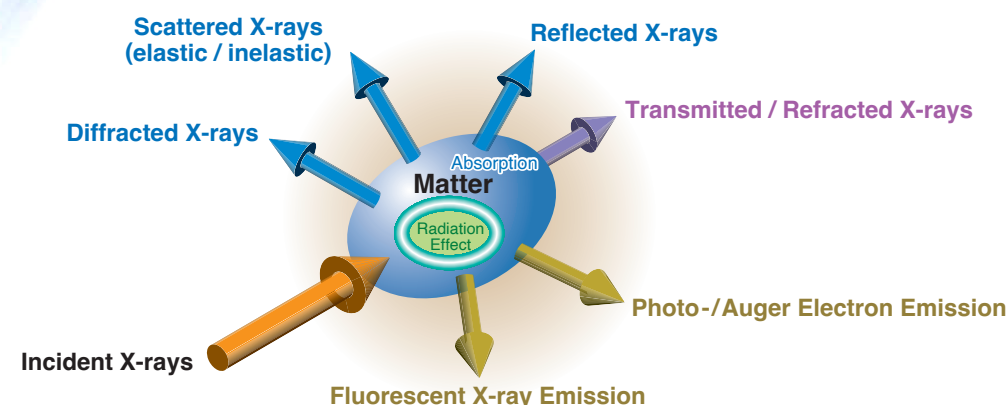
SPring-8 produces light that is about one billion times more brilliant than conventional X-ray sources.



▲ Synchrotron radiation produced at an undulator

Contribution to Advanced Research

Interaction of X-rays with Matter



Utilization of the Features of the SR Beam

- 1) With the use of the microbeam, diffractometry of very small samples and microscopy with high spatial resolution are carried out.
- 2) Time-resolved experiments are conducted on various time scales using the pulsed beam.
- 3) Energy tunability of the beam is effectively applied, for example, to crystal structure analysis using anomalous dispersion.
- 4) By making use of the highly collimated beam, various types of imaging techniques with high spatial resolution are developed.
- 5) The linearly / circularly polarized beam is used especially for studies on the magnetic properties of materials.
- 6) The availability of the high energy X-ray beam enables high-Q experiments, Compton scattering, excitation of high-Z atoms and nuclear excitation of isotopes.
- 7) With the use of the highly coherent beam, X-ray phase optics and X-ray interferometry are studied.

Application of SR to Various Scientific and Technological Fields

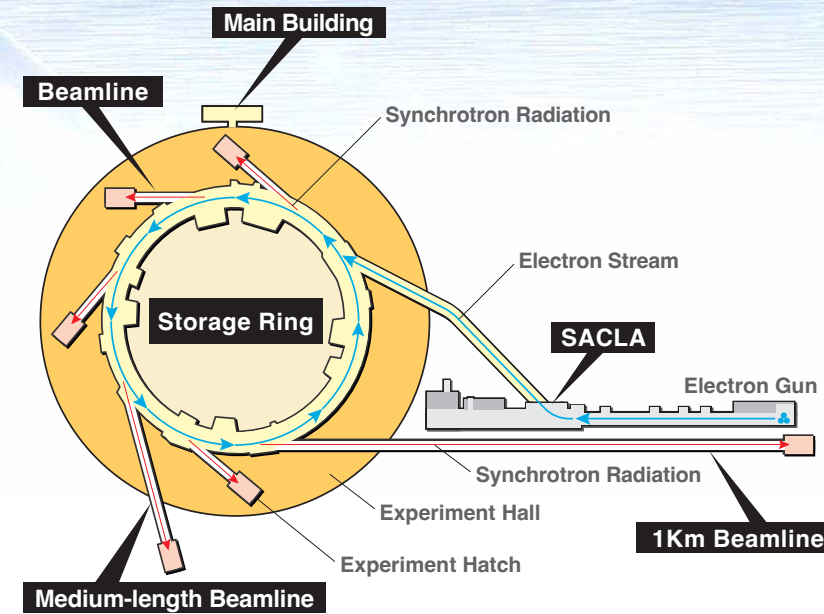
Synchrotron radiation is very useful for various fields in both basic and applied research. Synchrotron radiation available in SPring-8 is applied to the following advanced research fields.

- Life Science** : Atomic structure analysis of protein macromolecules and elucidation of biological functions. Mechanism of time-dependent biological reactions. Dynamics of muscle contraction.
- Materials Science** : Precise electron distribution in novel inorganic crystals. Structural phase transition at high pressure / high or low temperature. Atomic and electronic structure of advanced materials of high T_c superconductors, highly correlated electron systems and magnetic substances. Local atomic structure of amorphous solids, liquids and melts.
- Chemical Science** : Dynamic behaviors of catalytic reactions. X-ray photochemical process at surface. Atomic and molecular spectroscopy. Analysis of ultra-trace elements and their chemical states. Archeological studies.
- Earth and Planetary Science** : *In situ* X-ray observation of phase transformation of earth materials at high pressure and high temperature. Mechanism of earthquakes. Structure of meteorites and interplanetary dusts.
- Environmental Science** : Analysis of toxic heavy atoms contained in bio-materials. Development of novel catalysts for purifying pollutants in exhaust gases. Development of high quality batteries and hydrogen storage alloys.
- Industrial Application** : Characterization of microelectronic devices and nanometer-scale quantum devices. Analysis of chemical composition and chemical state of trace elements. X-ray imaging of materials. Residual stress analysis of industrial products. Pharmaceutical drug design.
- Medical Application** : Application of high spatial resolution imaging techniques to live animals and pathological samples.
- Nuclear Physics** : Quark nuclear physics by GeV photons, astronuclear process and photo nuclear reactions by MeV photons.

Main Facilities of SPring-8

● Generation of Synchrotron Radiation

The electrons emitted by the SACLA electron gun are accelerated to 8 GeV (8 billion electron volts) by the SACLA accelerator, injected into a storage ring with a circumference of about 1,500 m, and circulated while maintaining the energy of 8 GeV. Synchrotron radiation is generated by the bending magnets or insertion devices. The generated synchrotron radiation (X-rays) is guided through the beamline to the experimental hatches provided inside and outside of the storage ring building, and is used for various experiments.



■ Experimental Stations



Experimental Station in Experimental Hall
Synchrotron radiation from a bending magnet or an insertion device is modified with optics and led to the experimental station. A sample is studied by measuring X-ray scattering / diffraction, X-ray absorption, fluorescence X-rays, secondary electrons, and so on.

● Research Methods Used in the SR Science

X-ray Diffraction and Scattering

Research Method	Typical Examples of Research Subjects
Macromolecular crystallography	Atomic structure and function of proteins.
X-ray diffraction under extreme conditions	Structural phase transition at high pressure / high or low temperature.
X-ray powder diffraction	Precise electron distribution in inorganic crystals.
Surface diffraction	Atomic structure of surfaces and interfaces.
Small angle scattering	Structure of protein molecules and polymers.
Residual stress analysis	Three-dimensional strain mapping in bulk materials. Depth strain profiling.
X-ray Optics	X-ray interferometry. Coherent X-ray optics. X-ray quantum optics.

Spectroscopy and Spectrochemical Analysis

Photoelectron spectroscopy	Electronic structure of advanced materials.
Atomic and molecular spectroscopy	Photoionization, photoabsorption and photoelectron spectra of neutral atoms and simple molecules.
Compton scattering	Momentum distribution of electrons in materials and magnetic electrons.
X-ray inelastic scattering	Electronic excitation. Electron correlations in the ground state. Phonon excitation.
Nuclear resonant scattering	Time-domain Mössbauer spectroscopy. Nuclear inelastic scattering.
X-ray fluorescence spectroscopy	Ultra-trace element analysis. Chemical states of trace elements. Archeological and geological studies.
XAFS (X-ray absorption fine structure)	Atomic structure and electronic state around a specific atom.
X-ray magnetic circular dichroism	Magnetic properties of solids, thin films and surfaces. Orbital and spin magnetic moments.
Photon correlation spectroscopy	Speckle from disordered systems. Dynamics of atomic-scale disorder.
Infrared spectroscopy	Infrared microspectroscopy. Infrared reflection and absorption spectroscopy.

X-ray Imaging

Refraction-contrast imaging	Imaging of low absorbing specimens.
Phase-contrast imaging	Imaging of biological samples with an X-ray interferometer or gratings.
X-ray microtomography	Three-dimensional imaging.
X-ray fluorescence microscopy	Imaging of trace elemental distribution with a scanning X-ray microprobe.
X-ray microscopy	Imaging of materials by magnifying with microfocusing elements.
X-ray topography	Static and dynamic processes of crystal growth, phase transition and plastic deformation in crystals.
Photoelectron emission microscopy (PEEM)	Element-specific surface morphology. Chemical reaction at surface. Magnetic domains.

Radiation Effect

Material processing	Solid phase crystallization. Soft X-ray CVD. Microfabrication.
Radiation biology	Radiation damage of biological substances.

● Synchrotron Radiation Source and Beamlines

■ Undulator



There are two types of light sources in SPring-8. Those are insertion device source and bending magnet one. Insertion devices are classified into an undulator and a wiggler.

SPring-8 Beam Ports

- Insertion Device Beamlines (Straight Section 4.5m) max.34
- Long Insertion Device Beamlines (Long Straight Section 25m) max.4
- Bending Magnet Beamlines max.24

An undulator and a wiggler are composed of magnet arrays and produce periodic magnetic fields that wiggle electron beam and emit synchrotron radiation. In-vacuum type undulators developed at SPring-8 seal magnet arrays in a vacuum chamber. This arrangement results in a smaller gap between arrays. Therefore, synchrotron radiation with shorter wavelength and higher power can be generated.

■ Bending Magnet



Other than standard in-vacuum type, in-vacuum revolver undulator, invacuum figure-8 undulator, twin helical undulator, tandem vertical undulator, elliptical wiggler, and others are installed in SPring-8. These insertion devices generate various polarized radiation.

A bending magnet is a part of the storage ring that bends the electron orbit and emits white X-rays with the characteristic photon energy of 28.9 keV.

Mechanism of Water-Splitting Reaction in Photosynthesis

The water-splitting and oxygen-evolving reaction in photosynthesis is extremely important as it supports the lives of oxygen-breathing organisms on earth by converting light energy into chemical energy used by these organisms and supplies oxygen to the atmosphere. This reaction is carried out by a membrane protein complex called photosystem II. The cyanobacterial photosystem II consists of 17 transmembrane proteins and three peripheral membrane proteins, and forms a dimer with a molecular weight of 350 kDa for each of the monomers. The crystal structure of this dimer was analyzed at a resolution of 1.9 Å using the synchrotron radiation at SPring-8 (Fig. 1, left). As a result, not only the structure of each subunit and the organization of components contributing to the electron transfer are revealed, but also the detailed structure of the catalyst for the water-splitting and oxygen-evolving reaction contained in the dimer is clarified. This catalyst has a composition of Mn_4CaO_5 and resembles the shape of a "distorted chair", with Mn_3CaO_4 forming a cubane-shaped "seat" and the fourth Mn ion connecting to the outside of the cubane by an oxo-oxygen (Fig. 1, right). One of the reasons for the distortion of the cubane shape is the long bond distance between one of the five oxygen atoms, called O5, and the surrounding Mn ions. This observation suggests the possibility that O5 is located in a special position and is cut out during reaction, serving as one of the substrate oxygen atoms for the formation of the oxygen molecule. To demonstrate this, the intermediate states of the water-splitting reaction (S_2 and S_3 states) were generated by flash irradiation and observed in a pump-probe experiment conducted using the X-ray free electron laser at SACLA. The results showed that a new water molecule (O6) is inserted not in the S_2 state but in the S_3 state in a position close to O5, suggesting that an oxygen-oxygen bond is formed between O5 and O6, releasing molecular oxygen (Fig. 2).

BL41XU, BL45XU, SACLA

Jian-Ren Shen (Okayama University)

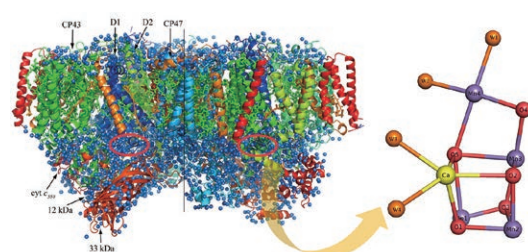


Fig. 1 Overall structure of photosystem II dimer (left) and structure of the Mn_4CaO_5 cluster (right).

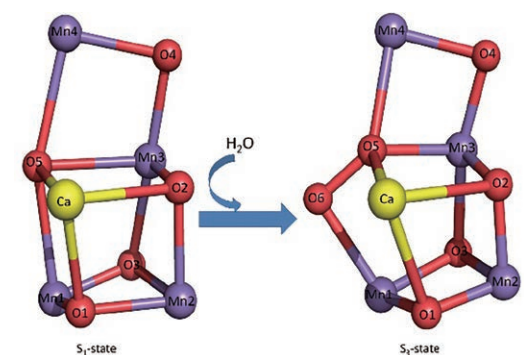


Fig. 2 Change in structure of Mn_4CaO_5 cluster during water-splitting reaction in photosystem II. The figure shows the structure in the S_1 state in the dark and that in the S_3 state generated by two-flash irradiation.

Protein density measurement in eye lens by phase-contrast CT

The eyeballs of vertebrates consist of soft tissues such as cornea, lens, retina. Since soft tissues do not absorb X-rays sufficiently, they are barely visible by X-ray absorption imaging methods such as radiography. However, by using the phase-contrast X-ray CT method that uses phase change of X-rays, each tissue can be clearly visualized (Fig. 1). In particular, the shape of the lens and the density distribution of major structural proteins (crystallins) within the lens can be measured with high precision. The protein density distribution can be converted via a linear equation to the refractive index which is distributed as a gradient and this determines lens refraction and provides high image quality needed by the eye. At SPring-8, BL20B2 is equipped with a device that can easily perform phase-contrast imaging using diffraction gratings. This method allows the most accurate measurements of refractive index of any methods available and is the only means of obtaining shape and refractive index profiles in 3-dimensions from intact lenses (Fig. 1). For example, in the human crystalline lens, the shape of the lens changes with age without much change in the maximum value and distribution of the refractive index (Fig. 2). Water channel proteins in the lens, the aquaporins, have been shown to be important for the formation of the shape of the normal lens in zebrafish. The technique is also the first to provide accurate measurements from lenses with opacifications. It has therefore made it possible for measurements of refractive index to be made in lenses with cataracts and has indicated how mutations in zebrafish lenses manifest as disturbances to the refractive index and how this can affect lens optics. In addition, it was found that the density distributions in the lenses of cataract model mice are different from those in wild type mouse lenses, and oxysterols, which have recently attracted attention as a compound that eliminates the opacity of the lens due to cataract, can restore normal density distribution. In this way, the high spatial and density resolution of phase-contrast X-ray CT is useful for studying the detailed structure and function of biological tissues.

BL20B2

Barbara Pierscionek (Anglia Ruskin University, UK)

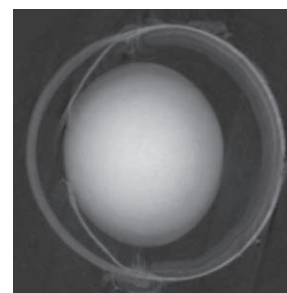


Fig. 1 Phase contrast image of a mouse eye showing eye lens

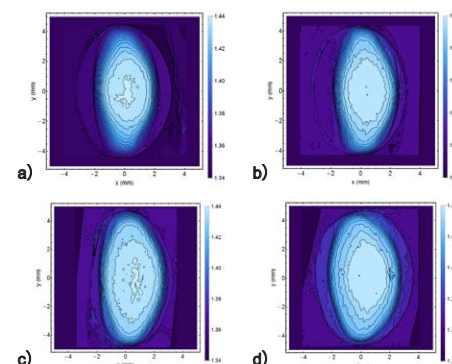


Fig. 2 Isoindicial contours of refractive index in human lenses aged a) 35 years, b) 48 years, c) 68 years and d) 86 years

Novel Drug Delivery System Using Cancer-Cell-Targeted Protein Nanocapsules

Small-angle X-ray scattering (SAXS) is an effective technique for obtaining submicron- to nanometer-scale structural information. SAXS can be measured in air with little limitation of the sample shape and measurement environment. A drug delivery system (DDS) is a system that encapsulates poorly water-soluble or easily degradable drugs into particles (nanocapsules) to solubilize or preserve the drugs, transports them to target cells through, for example, blood vessels, and releases them in the target cells. SAXS is suitable for studying the structure of DDS particles in solution. The objective of this study is to develop the DDS using lipocalin-type prostaglandin D synthase (L-PGDS), a biocompatible transport protein, as the particles. Although 7-ethyl-10-hydroxycamptothecin (SN-38) has high anti-tumor activity, it is not used in clinical practice because of its poor water solubility. We therefore tried to solubilize SN-38 by encapsulating it into L-PGDS and clarified the changes in the structure of L-PGDS with encapsulated drugs by SAXS performed at BL40B2. The scattering curves obtained by SAXS showed that the overall structure of L-PGDS is spherical and that L-PGDS does not coagulate but is monodispersed even in solution (Fig. 1). Also, the radius of gyration (R_g) was obtained from the Guinier plot for the small-angle region in the scattering curves. The R_g of L-PGDS decreased when SN-38 was encapsulated into it (Fig. 2). These results showed that L-PGDS is a very flexible protein that becomes compact when SN-38 is encapsulated into it.

BL40B2 Masatoshi Nakatsuji, Takashi Inui (Osaka Metropolitan University)

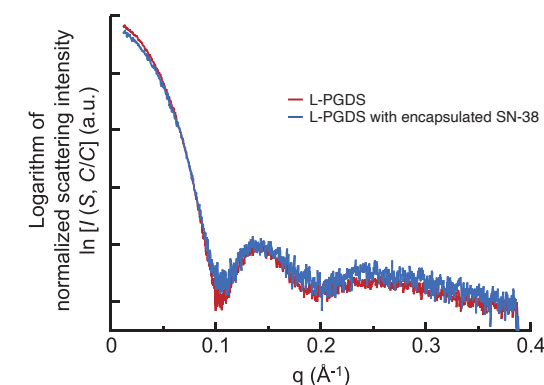


Fig. 1 Scattering curves of L-PGDS and L-PGDS with encapsulated SN-38

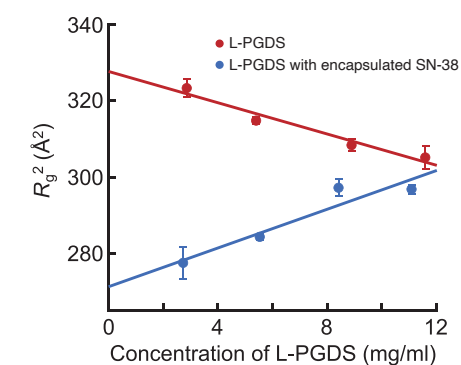


Fig. 2 L-PGDS concentration dependence of R_g^2 obtained by Guinier plot for L-PGDS with encapsulated SN-38

Intratumor Distribution of Very Small Amounts of Anticancer Drug Visualized via High-Intensity Nanobeam at SPring-8

Oxaliplatin (L-OHP), a third-generation platinum complex antitumor drug, is widely used in the treatment of colorectal cancer. However, L-OHP is effective in ~50% of the patients with advanced/recurrent colorectal cancer. Moreover, the use of L-OHP causes adverse effects such as neutropenia and peripheral sensory neuropathy. Establishing techniques to predict and evaluate the therapeutic effects of this drug is desired for achieving an effective and safe chemotherapy regimen. We therefore quantitatively analyzed and visualized the distribution of the platinum contained in L-OHP and essential metals by synchrotron radiation X-ray fluorescent spectrometry (SR-XRF) analysis to human cancer tissues and examined how this distribution is related to the effectiveness of chemotherapy and clinicopathological factors.

In the SR-XRF analysis of 30 rectal cancer specimens resected from patients who received L-OHP-based preoperative chemotherapy, the platinum concentration in the cancer tissue was 2.85–11.44 ppm (lower detection limit: 1.848 ppm). In the tumor epithelium, the concentration of accumulated platinum was significantly higher in the areas showing marked improvement by chemotherapy than in other areas. Conversely, in the tumor stroma, the concentration of accumulated platinum was higher in patients with limited effects of chemotherapy. The results of multivariate analysis showed that the concentration of accumulated platinum in the tumor stroma is an independent predictive factor of therapeutic effects. The results of principal component analysis suggested that copper transporters contribute to drug resistance.

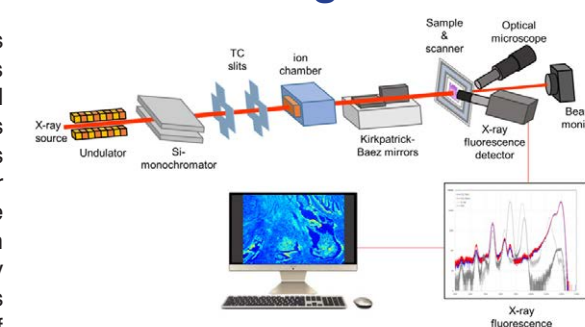
BL37XU Maiko Nishibori, Hayato Fujita, Ryo Koba (Kyushu University)
Article: R. Koba *et al.*: *Int. J. Cancer*, **146** (9), 2498-2509 (2020)

Fig. 1 Schematics of XRF analysis apparatus.

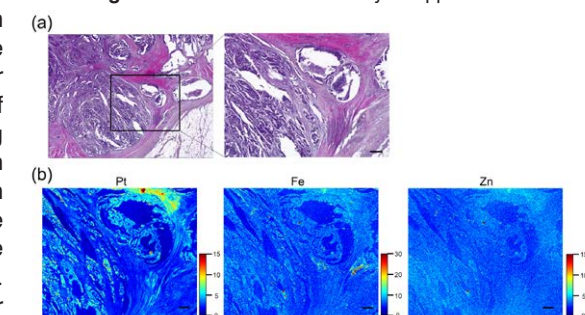
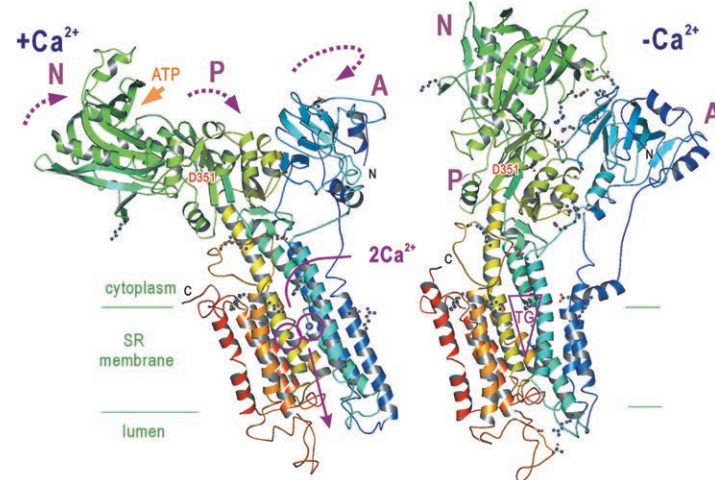


Fig. 2 (a) Representative histopathologic image of rectal cancer section. The image on the right is an enlarged view of the square in the image on the left. (b) XRF mapping of platinum, iron, and zinc in the same sample.

Insight into the mechanism of active transport by calcium pump

SPring-8 played a vital role in the recent structure determinations of the sarcoplasmic reticulum (SR) calcium pump in the calcium bound and unbound states. The ATP-driven calcium pump is an integral membrane protein (molecular weight of 110 k) that relaxes muscle cells by pumping calcium released during contraction back into the sarcoplasmic reticulum. The crystals were thin (<20 μm; Ca²⁺-bound form) or had a very large unit cell dimension (nearly 600 Å; Ca²⁺-unbound form). Hence, the use of very bright and highly parallel X-ray beam available in undulator beamlines, such as BL41XU (Structural biology I) and BL44XU (Protein Institute, Osaka University), were essential to these structure determinations.

These studies have revealed that the binding of calcium alone accompanies a surprisingly large-scale rearrangement of both transmembrane and cytoplasmic domains, and that the ion pumps work like mechanical pumps at an atomic scale. Also, the structure of a very strong inhibitor, thapsigargin (TG), bound to this pump was determined and may serve as a template for drugs targeted for membrane proteins. Calcium is a fundamental and ubiquitous factor in the regulation of intracellular processes. Therefore, the atomic structures of the calcium pump in different states have a tremendous impact on many fields, including medical treatment for myocardial diseases and cancer.



BL41XU Chikashi Toyoshima (University of Tokyo)

Structural change of calmodulin molecule caused by calcium binding

Calmodulin is a small protein with a molecular weight of 17,000 that is expressed in almost all eukaryotic cells and plays a role of transporting intracellular information. When the calcium concentration in the cell is increased by an external stimulation, calmodulin binds calcium ions and then binds to other proteins such as enzymes, and causes various changes in the cell. Upon binding calcium, the structure of the calmodulin molecule changes, allowing it to bind to other proteins. X-ray crystallography revealed that the calmodulin molecule is extended in the absence of calcium, whereas it becomes globular upon binding calcium ions. However, this change occurs in a short time (milliseconds) and its details remained unclear. In this study, the structural change of the calmodulin molecule was clarified by the small-angle scattering technique using intense X-rays from the undulator beamline BL40XU.

When calmodulin molecules were dispersed in solution and the calcium concentration was rapidly increased using a chelating agent that released calcium upon laser irradiation, the radius of gyration (an indicator of molecular size) of the calmodulin molecules decreased by ~25% in ~10 ms (Fig. 1). This indicates that the calmodulin molecules bound calcium ions and became compact. When a peptide was present as a binding partner in the solution, the compact form was stabilized and maintained (Fig. 1, white). Without the binding partner, however, the calmodulin molecules returned to the original extended state in ~150 ms (Fig. 1, black).

The existence of the compact structure observed immediately after calcium binding (Fig. 2) was demonstrated for the first time. This structure corresponds to the crucial state in the transmission of the calcium signal by calmodulin molecules through binding to other proteins. This finding will lead to clarification of cellular functions and to development of agents that target these proteins.

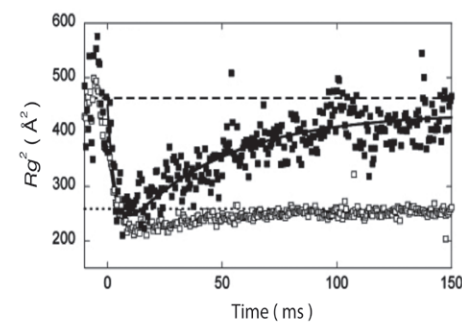


Fig. 1 Change in radius of gyration (Rg) of calmodulin molecules when calcium concentration was increased at time 0

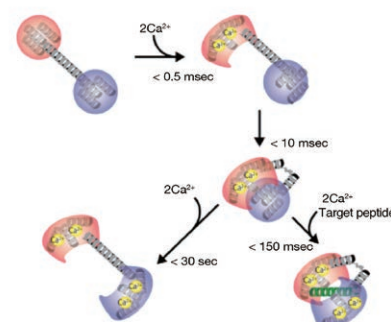


Fig. 2 Structural change of a calmodulin molecule upon calcium binding

BL40XU Yoshiteru Yamada, Hiroyuki Iwamoto, Naoto Yagi (JASRI)

Direct Observation of External Force-Induced Changes in Internal Structure of Steel Sheet for Next-Generation Vehicles —Development of Combined X-ray Computed Tomography Analysis Technique—

Transformation-induced plasticity (TRIP) steel is coming into use as the steel sheet for next-generation vehicles. It has a unique feature called “phase transformation”, namely, the change in metal structure caused by an external force. TRIP steel consists of ferrite and 20–30% of a metastable phase called retained austenite dispersed across the ferrite phase. The soft retained austenite phase is transformed to a hard martensite phase when an external force is applied. However, the phase transformation in TRIP steel must be observed and analyzed nondestructively because the phase transformation is easily induced even by grinding and machining. We developed a multimodal assessment technique by combining (1) X-ray nanotomography for the nondestructive, direct visualization of the phase transformation behavior in TRIP steel and (2) pencil-beam diffraction tomography for the measurement of crystallographic orientation and dislocation density. The spatial resolution of X-ray nanotomography is 0.16 μm, and the diameter of the X-ray beam used in pencil-beam diffraction tomography is 3 μm, which enables the observation and analysis of a very fine material structure. Figure 1 shows the schematics of the experimental setup. Switching between these methods takes 2–3 min and can be performed by just pressing a button. In this study, this technique was applied for the first time to the in situ observation of steel under external loading. As a result, the phase transformation, deformation, and rotation behaviors of individual austenite grains were clearly observed in three dimensions. Figure 2 shows the transformation behavior of a particular crystal grain for which the crystallographic orientation was determined. Previously, it was impossible to obtain design guidelines for the optimal microstructure because only average information from a wide area of steel could be achieved. However, the interactions between the individual retained austenite grains were directly visualized in this study, which provided clear guidelines for microstructure design.

The direct monitoring of phase transformation phenomena by the multimodal assessment technique will provide an accurate understanding of shock absorption and fracture properties, leading to a microstructure design for optimum shock absorption and fracture properties.

BL20XU Kyosuke Hirayama (Kyoto University), Hiroyuki Toda (Kyushu University)

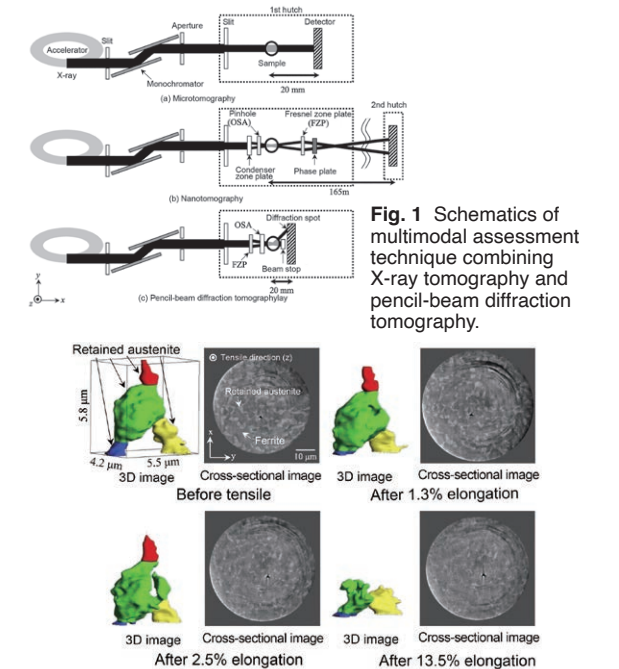


Fig. 1 Schematics of multimodal assessment technique combining X-ray tomography and pencil-beam diffraction tomography. Fig. 2 Phase transformation behavior of retained austenite grains. The figure also shows the transformation behavior in the cross-sectional images of the grain during the same loading steps. The transformation of retained austenite grains occurs locally but not uniformly.

Observing Instantaneous Dislocation in Steel During Ultrafast Heating

The heating and cooling rates during thermal treatment in the manufacturing of steel are extremely important parameters that determine the properties of these materials. However, the physical and kinetic understanding of atomic diffusion and structural changes with rapid changes in temperature has not yet been clarified because of difficulties in their observation. In particular, for the development of manufacturing techniques for high-quality materials, it is crucial to understand and precisely control dislocations (crystal defects) during microstructural changes from martensite to austenite (phase transformation). The ultrafast structural changes caused by an extreme increase in temperature are unknown. Important insights can be gained by observing these changes that will lead to the production of high-performance and high-quality steel. Although dislocations have been observed at a heating rate of 2–3 °C/s, it has been difficult to observe the fast microstructural changes at high temperatures where atomic diffusion is rapid. Therefore, the dislocation during the formation of austenite from martensite has not been clarified.

In this study, an originally designed ultrafast heating and cooling system was installed at the world’s most advanced X-ray free electron laser facility, SACLA. Structural changes in martensite at a heating rate higher than 10,000 °C/s were observed by femtosecond X-ray diffraction. The instantaneous dislocation during the ultrafast heating of the martensite structure in steel was quantitatively observed for the first time in the world (Fig. 1). The microstructure formation process was clarified from the perspectives of dislocation density and carbon concentration (Fig. 2). The *in situ* observation of the dislocation and carbon concentration related to microstructure formation in steel will lead to improvements in the performance and quality of steel, the development of new alloys or new manufacturing processes, and other major breakthroughs.

SACLA BL3 Mitsuharu Yonemura (Nippon Steel Corporation) Article: M. Yonemura *et al.*, *Scientific Reports* 9, 11241 (2019).

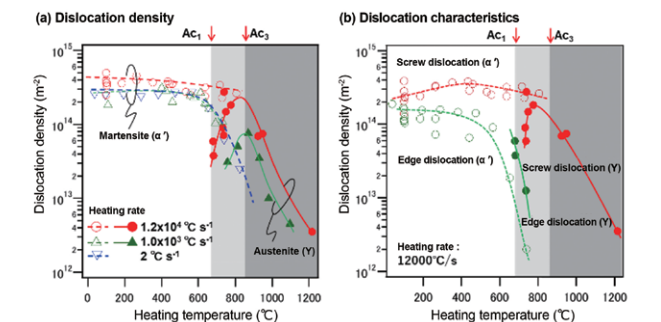


Fig. 1 Changes in dislocation density and dislocation characteristics during heating.



Fig. 2 Structural changes during ultrafast heating.

Observing Hidden Electronic States of Trace Elements

Rare-earth elements are used in various highly functional materials. Recently, the exploration and recovery of natural resources containing rare-earth elements have become important issues. Analytical techniques for elements contained in natural minerals are limited, especially when those elements are present in trace amounts. For example, the direct detection of the electronic state of europium (Eu) in natural samples has been impossible by conventional techniques because the Eu content of a crustal material is generally 1 mg/kg or less. Such a detection limit is determined not by Eu concentration but by the superposition with high fluorescence emissions from manganese (Mn) contained in the same natural samples. The separation of the fluorescence emission of Mn from that of Eu is therefore necessary to determine the electronic state of Eu.

X-ray emission spectroscopy (Fig. 1) is a technique for observing fluorescent X-rays with a high energy resolution. Using this technique, it is possible to extract the fluorescent X-rays from trace elements that could not be observed using a semiconductor detector capable of energy-dispersive analysis that is used for conventional fluorescent X-ray analyses. Also, with its high energy resolution, X-ray emission spectroscopy provides a spectral structure that is clearer than the conventional X-ray absorption near-edge structure (XANES), enabling the detailed observation of electronic states. In this study, issues with conventional XANES measurements were resolved using X-ray emission spectroscopy. The Eu valence in a common rock-forming mineral, potash feldspar, with a Eu concentration of 5 ppm or lower was determined by high-energy resolution fluorescence detection (HERFD)-XANES measurement. The sample used here was JF-1, a standard rock issued by Geological Survey of Japan (GSJ), prepared from natural feldspar (Ohira feldspar) in Nagiso, Nagano, Japan (Fig. 2).

BL39XU Rimi Konagaya, Yoshio Takahashi (The University of Tokyo)
Article: R. Konagaya *et al.*, *Chem. Lett.* **50**, 1570 (2021)

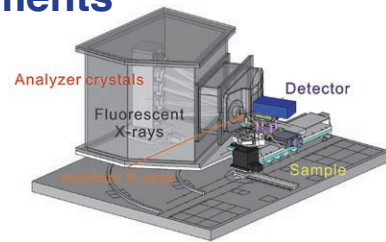


Fig. 1 Schematic diagram of X-ray emission spectrometer. The fluorescent X-rays from the sample are dispersed and focused with a high energy resolution using an analyzer crystal. Their intensity is measured using the detector.

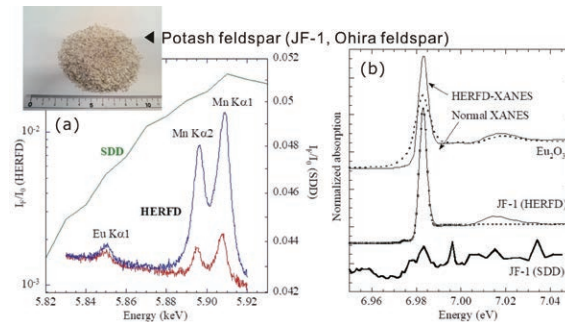


Fig. 2 (a) Fluorescent X-ray spectra of JF-1 sample obtained using semiconductor detector (SDD) and X-ray emission spectroscopy (HERFD). (b) XANES spectra of JF-1 sample obtained using SDD and HERFD.

Clarifying Crystal Structure of Sulfur Hydride Exhibiting High-Temperature Superconductivity under Ultrahigh Pressure

Some materials do not exhibit superconductivity at ambient pressure but become superconductors under high pressure. Among those materials, hydrogen and hydrogen-rich compounds have for many years been expected to become room-temperature superconductors under ultrahigh pressure. Recently, hydrogen sulfide (H₂S) has been found to have a superconducting transition temperature T_c of -73°C under an ultrahigh pressure of 150 GPa. Such a T_c value eclipsed the previous highest T_c of a copper-oxide superconductor, HgBa₂Ca₂Cu₃O_y (Fig. 1▲), by more than 30°C and exceeded the lowest temperature on Earth's surface (-93°C). Hydrogen sulfide is a pioneering hydrogen-rich compound, which exhibits high-temperature superconductivity under high pressure. However, its crystal structure, which is important for understanding the mechanism of its superconductivity, has remained unknown. In this study, the crystal structure of the high- T_c phase was investigated by the simultaneous measurements of powder X-ray diffraction and electrical resistance in a pressure range of 110–190 GPa and a temperature range from room temperature to -263°C at the high-pressure research beamline BL10XU in SPring-8. Hydrogen sulfide is composed of light elements, sulfur and hydrogen, and the sample is very small (less than 30 μm in diameter) and thin for ultrahigh-pressure generation. Therefore, the high-luminosity and high-energy (30 keV) X-ray focused on a half bandwidth of 2 μm available at BL10XU is very effective for analyzing the distribution of a microscale sample in a pressure-generating device called a diamond anvil cell (Fig. 2). In this study, it was clarified for the first time in the world that the high- T_c phase is H₃S with sulfur atoms arranged in a body-centered cubic structure (Fig. 1, right) and that hydrogen sulfide, H₂S, molecularly dissociates into H₃S and sulfur under high pressure.

Hydrogen sulfide is a pioneering hydrogen-rich compound, which exhibits high-temperature superconductivity under high pressure. However, its crystal structure, which is important for understanding the mechanism of its superconductivity, has remained unknown. In this study, the crystal structure of the high- T_c phase was investigated by the simultaneous measurements of powder X-ray diffraction and electrical resistance in a pressure range of 110–190 GPa and a temperature range from room temperature to -263°C at the high-pressure research beamline BL10XU in SPring-8. Hydrogen sulfide is composed of light elements, sulfur and hydrogen, and the sample is very small (less than 30 μm in diameter) and thin for ultrahigh-pressure generation. Therefore, the high-luminosity and high-energy (30 keV) X-ray focused on a half bandwidth of 2 μm available at BL10XU is very effective for analyzing the distribution of a microscale sample in a pressure-generating device called a diamond anvil cell (Fig. 2). In this study, it was clarified for the first time in the world that the high- T_c phase is H₃S with sulfur atoms arranged in a body-centered cubic structure (Fig. 1, right) and that hydrogen sulfide, H₂S, molecularly dissociates into H₃S and sulfur under high pressure.

BL10XU Mari Einaga (Osaka University)

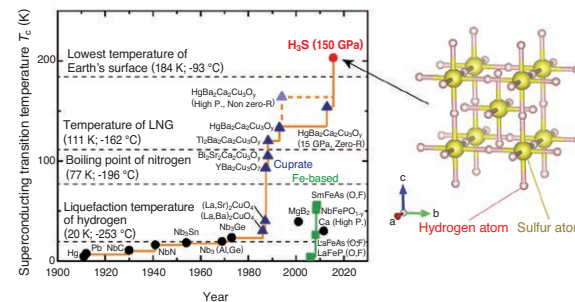


Fig. 1 (Left) Temporal evolution of the superconducting transition temperature T_c and (right) predicted crystal structure of the high-temperature superconducting phase (high- T_c phase) of H₃S.

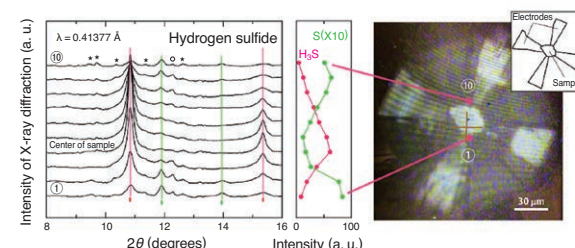


Fig. 2 (Left) Sample distribution in a pressure device obtained by X-ray scanning and (right) the microscopic image of the vicinity of the sample at 150 GPa. The result of this scanning indicates that there is a large amount of H₃S near the center of the sample.

Clarifying 3D Atomic Arrangement of Dopant in Diamond

Diamond is an important material not only for its beauty as a gem but also for its excellent properties such as high hardness, high thermal conductivity, and good insulating performance. Diamond is attracting attention from the perspective of element strategy in Japan, a resource-limited country, because it is a crystal of carbon, a common element. Diamond, with its good insulating performance, is a promising material for realizing next-generation power devices and quantum sensors because it becomes a high-performance semiconductor when doped with small amounts of other elements. For device applications, it is necessary to introduce electrons or holes (electron vacancies) into diamond by doping to make it conductive. p-type semiconductors can be synthesized by boron doping, whereas n-type semiconductors can be synthesized by phosphorus doping. Improvements in the quality of those semiconductors will be an important factor that determines device performance.

In this study, ultrahigh-precision photoelectron holography was performed on a phosphorus-doped n-type diamond film (phosphorus concentration: 0.06 at.%; provided by Dr. Hiromitsu Kato of AIST) fabricated by chemical vapor deposition (Fig. 1). The 3D atomic arrangement of elemental phosphorus in diamond, which could not be observed by conventional techniques such as electron microscopy and X-ray crystal structure analysis, was clarified for the first time in the world. Doped phosphorus atoms are incorporated into diamond in the following two structures: (a) a structure where a carbon atom of diamond is substituted by a phosphorus atom (lattice substitution) and (b) a structure where two adjacent carbon atoms are removed and a phosphorus atom is located between two carbon-atom sites. Whereas (a) is an electrically active structure emitting electrons in the diamond crystal, (b) is an inactive structure capturing electrons. It was also observed that (b) is a structure oriented in the diamond growth direction. The atomic arrangement of phosphorus and the electrical activation state in diamond were thus “visualized”. Advanced strategies for sample preparation, such as increasing the concentration of the active structure while suppressing the inactive structure, can be developed by changing the crystal growth conditions of diamond and observing the changes in its structure during measurements.

BL25SU Takayoshi Yokoya (Okayama University), Tomohiro Matsushita (Nara Institute of Science and Technology)
Article: T. Yokoya *et al.*, *Nano Letters* **19**, 5915 (2019)

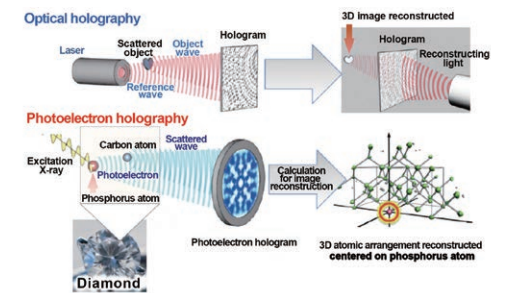


Fig. 1 Conceptual diagram of photoelectron holography.

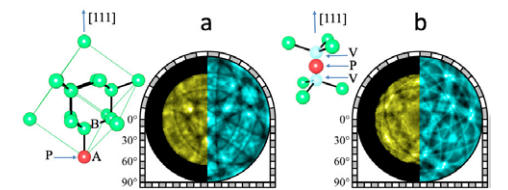


Fig. 2 Photoelectron hologram and reconstructed atomic arrangement of phosphorus in diamond.

Capturing atomic movement of millionths of a second

Piezoelectric crystals contract and deform macroscopically upon the application of an electric field. This phenomenon was discovered by J. Curie and P. Curie in the late 19th century. Nowadays, piezoelectric devices based on this phenomenon are used in various applications such as the control of ink ejection of printers and the touch panels of cell phones; thus, piezoelectric devices are indispensable in our daily lives. Although various mechanisms behind the significant deformation of the exterior of piezoelectrics have been discussed, the process from voltage application to the displacement of atoms in the crystal at the micron level should be examined to understand the fundamentals of the mechanism. However, this atomic displacement is extremely small and difficult to detect. Therefore, even the movement of crystal lattices has remained unclarified thus far.

In this study, the research group succeeded, for the first time in the world, in the in situ observation of the time-course change in the lattice of a piezoelectric crystal that underwent piezoelectric vibration on the order of microseconds. This was achieved by combining two advanced measurement techniques: precision crystallography and high-speed time-resolved measurement at SPring-8 BL02B1 (Fig. 1). The research group is the first ever to observe that an expanded crystal lattice, owing to the application of an electric field, deformed as if it were a spring undergoing damped vibration (Fig. 2). In addition, we observed an interesting phenomenon that the crystal lattice contracted once during the polarization reversal that occurred immediately before the crystal lattice greatly expanded.

The above achievements are expected to promote research on the nano- or picosecond-order dynamics of atomic displacement and to enable the “fluoroscopic” observation of the behavior of the atoms in working electronic devices. Moreover, the measurement techniques used in this study can be applied to the development of new materials for electric storage devices such as capacitors and batteries.

BL02B1 Chikako Moriyoshi, Yoshihiro Kuroiwa (Hiroshima University)

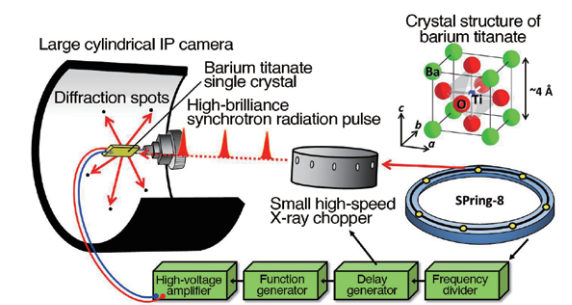


Fig. 1 Time-resolved X-ray diffraction experiment using synchrotron radiation pulses at SPring-8

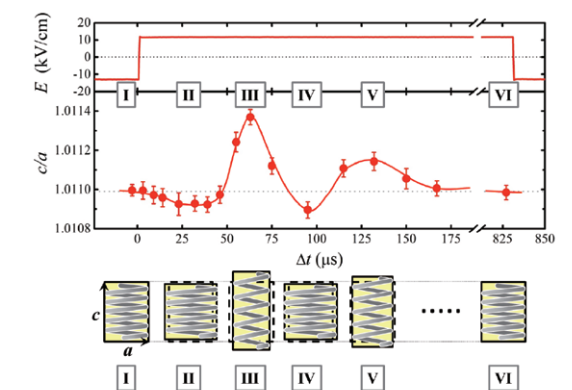


Fig. 2 Dynamic response of piezoelectric crystal to applied voltage

Visualization of large cage-like network structure of glass and solvated electrons

Generally, glass is formed by melting a raw material to a melt (liquid) state at high temperature followed by cooling. Not all materials can be made into glass; many materials form crystals instead of glass when a melt is cooled. To understand the glass formation of materials, the research group focused on CaO-Al₂O₃ systems that form or do not form glass depending on slight differences in the composition (material with a high glass-forming ability: 64 mol%CaO-36 mol%Al₂O₃; material with a low glass-forming ability: 50 mol%CaO-50 mol%Al₂O₃). To form glass using a material with a low glass-forming ability, the material was maintained as a melt without a container (containerless processing) and then rapidly cooled to form glass (Fig. 1). The atomic structures of the glasses were examined by high-energy X-ray scattering and X-ray absorption fine structure (XAFS) at SPring-8 (Fig. 2). The data were analyzed by large-scale theoretical calculations using a supercomputer to determine the atomic and electronic structures of the glasses. The results indicate that a large "cage-like network structure" (Fig. 3) forms in the materials with a high glass-forming ability. In contrast, such a structure does not exist in the materials with a low glass-forming ability. Researchers have recently reported that electrified glass can be formed by solvated electrons through the removal of oxygen in a reducing atmosphere. The solvated electrons are located in the cage-like network structure and were found to lead to an energetically stable glass structure by the large-scale theoretical calculation.

BL01B1, BL04B2

Shinji Kohara (NIMS)



Fig. 1 Oxide melt levitated at high temperature (by courtesy of Atsunobu Masuno, The University of Tokyo)

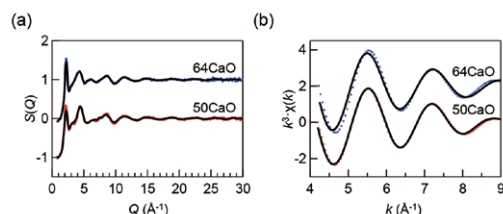


Fig. 2 Results of (a) high-energy X-ray scattering and (b) XAFS at Ca K absorption edge (blue and red dots) shown with the results of large-scale theoretical calculation (black lines)

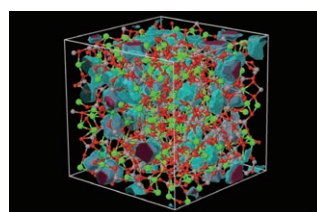


Fig. 3 Atomic arrangement of the 64 mol%CaO-36 mol%Al₂O₃ material with a high glass-forming ability

Successful fabrication and structural determination of crystal-oriented nanofilm of porous coordination polymer

Porous coordination polymers (PCPs) are material groups that exhibit high gas adsorption/separation properties and high regularity (crystallinity) and have various functions, such as high-efficiency separation and concentration of gas molecules and specific reactions inside the pores. Therefore, integrating PCPs with different functionalities enables the fabrication of various energy-related devices, such as highly efficient fuel cells. To develop such devices, multiple PCP nanofilm should be grown in the same direction (i.e., oriented growth) so that the different PCPs can be closely integrated. Thus far, however, the fabrication of crystal-oriented nanofilm has been successful only for two-dimensional PCPs. A technology for realizing the oriented growth of three-dimensionally rigid PCP crystals has long been demanded for increasing the functional diversity, the device durability, and the adhesion between different PCPs during integration.

In this study, a crystal-oriented nanofilm of three-dimensionally rigid PCP has been successfully fabricated by appropriately selecting a metal substrate suitable for oriented growth, a surface processing method of the substrate, and building blocks that can be controlled in terms of the growth direction while maintaining their rigidity in three dimensions (Fig. 1). In addition, the reversible gas adsorption/desorption behavior was observed in this nanofilm, and this behavior does not involve any change of the skeletal structure, reflecting the rigidity of this nanofilm. The observation of the oriented growth of the nanofilm and its structural change during the gas adsorption/desorption process was achieved using high-brilliance X-rays and the measurement system installed on the BL13XU beamline of SPring-8, which enables precise diffraction experiments of surfaces and interfaces (Fig. 2).

The results of this study are the basis of fundamental technologies for fabricating new functional devices that integrate PCPs with different functionalities. The research and development of functional devices using nanocrystalline thin films will be greatly accelerated and various applications such as highly efficient fuel cells are expected.

BL13XU

Kazuya Otsubo, Hiroshi Kitagawa (Kyoto University)

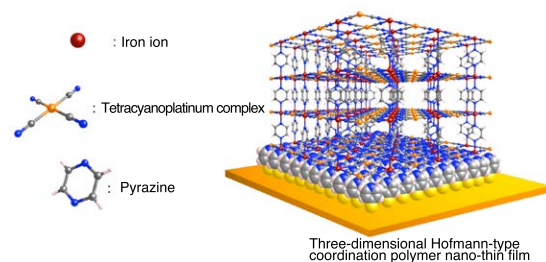


Fig. 1 Grown three-dimensionally oriented PCP nanocrystalline thin film

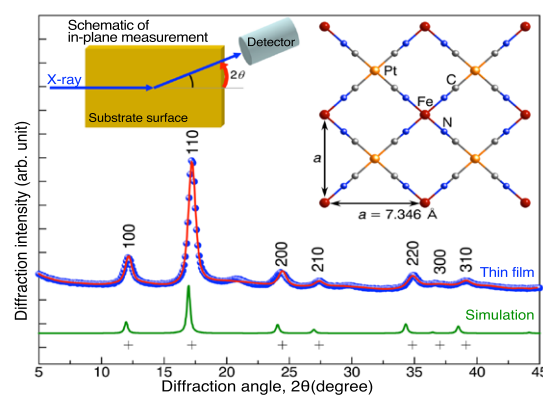


Fig. 2 Synchrotron radiation X-ray diffraction profile of grown three-dimensionally oriented PCP nanocrystalline thin film

Large Amount of Hydrogen Existing in Earth's Core

— Primitive Earth Contained About 50 Times as Much Water as Current Amount of Seawater —

It has been known for 70 years that large amounts of light elements (elements with a low atomic number) other than iron and nickel are contained in the metallic core at the center of the Earth. The density of the liquid core (outer core) is 8% smaller than that of liquid iron; this difference is called the density deficit. However, the core light element composition has been a great mystery of Earth science. We have been performing X-ray diffraction measurements under high pressure and high temperature, which simulate the conditions deep inside the Earth's interior using a device called a diamond-anvil cell (Fig. 1) at the high-pressure research beamline (BL10XU). Recently, we have found that most of water on the growing Earth was incorporated into the core as hydrogen when metallic iron moved toward the center of the Earth to form the core (Fig. 2). This observation suggests that hydrogen is the main light element in the core. An amount of water at least equal to the amount of seawater on the Earth's surface exists in the rock of the mantle of the present Earth. Considering that the amount of water not incorporated into metals is approximately twice the amount of seawater, the core should contain 0.3–0.6 wt% of hydrogen. Such amount of hydrogen would account for 30–60% of the density deficit of the outer core. It is also likely that a large amount of water has been incorporated as hydrogen in the core of not only the Earth but any terrestrial (rocky) planet having a mass exceeding 10% of the Earth, such as Mars. The large amount of hydrogen in the Earth's core must originally have existed as water, the amount of which is equivalent to 40–70 times the current amount of seawater. It is considered that such a large amount of water was brought from outside of the solar system (from the current asteroid belt or further outside) during the growth of the primitive Earth. Organic substances must also have been brought to the Earth with water. Studies are being carried out to find the location on the Earth of the carbon in these organic substances.

BL10XU

Kei Hirose (The University of Tokyo)

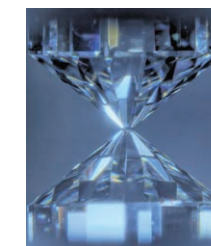


Fig. 1 High-pressure generating device using diamond anvils. A high pressure is applied to a sample using two diamond tips. A high temperature is achieved by irradiating the sample with a laser. The state of the minute sample under high pressure and high temperature can be analyzed by X-ray diffraction measurements.

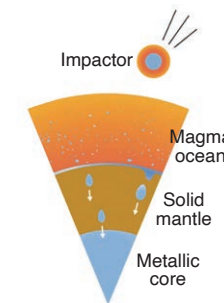


Fig. 2 Process of metallic core formation during Earth accretion. The Earth at that time was covered with a magma ocean. The metals contained in the substances (impactors) newly accumulated on the Earth fell like raindrops through the magma ocean while moving toward the center of the Earth. The water contained in the magma was incorporated into the metals as hydrogen.

Formation and Evolution of Carbonaceous Asteroid Ryugu: Evidence Obtained by CT Imaging of Returned Samples

Samples of the carbonaceous asteroid Ryugu were brought to Earth by the asteroid exploration spacecraft Hayabusa2 in December 2020. As part of the initial analysis of the returned samples, we investigated the formation and evolution process of the asteroid Ryugu by performing a multiscale, non-destructive, three-dimensional analysis that combined different X-ray computed tomography (CT) techniques available at SPring-8. The returned samples were black particles ranging 10 μm–8 mm in size (Fig. 1). The three dimensional images of the larger particles with a diameter of 100 μm or more and those of the particles smaller than 100 μm were obtained using the X-ray CT system at BL20XU and BL47XU, respectively. At BL20XU, the volume of the samples was accurately determined by CT imaging with a spatial resolution of 1 μm or less. The density of the samples was determined from the mass measured using an electronic balance (Fig. 1). These analyses were performed without exposure to air to avoid the contamination of the samples. The mean density of the samples was $1.79 \pm 0.08 \text{ g/cm}^3$, which is considerably higher than the density of the entire asteroid Ryugu (1.19 g/cm^3). This result indicates that the asteroid Ryugu contains pores accounting for at least 30% of its total volume. Consistent with this finding, Ryugu is an asteroid having a rubble-pile structure, namely, one formed by the accumulation of masses of rock generated by the collisional destruction of the parent body.

At BL47XU, CT imaging with a spatial resolution of ~100 nm was performed using two modes, imaging absorption-contrast CT and phase-contrast scanning-imaging CT, to investigate the three-dimensional spatial distribution of the substances composing the samples. We discovered fluid inclusion confined in a hexagonal iron sulfide crystal (Fig. 2). This fluid once existed on the parent body of Ryugu. When subjected to cryo time-of-flight scanning ion mass spectrometry (cryo-TOF-SIMS) analysis, the fluid was found to be carbonated and to contain salt and organic substances. This result suggests that the parent body of Ryugu formed in the low-temperature region of the solar system beyond Jupiter's orbit. The outcomes of this study provide important clues about how and where in the solar system carbonaceous asteroids formed, evolved, and were destroyed to achieve their present form.

BL20XU, BL47XU Megumi Matsumoto (Tohoku University), Akira Tsuchiyama (Ritsumeikan University), Masayuki Uesugi (JASRI) Article: T. Nakamura *et al.*, *Science* **379**, eabn8671 (2023). DOI: 10.1126 / science.abn8671

Optical microscopic image of C0002 particle

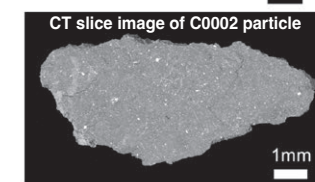


Fig. 1 Optical microscopic image and CT slice image of C0002 particle (third-largest particle collected by Hayabusa2)

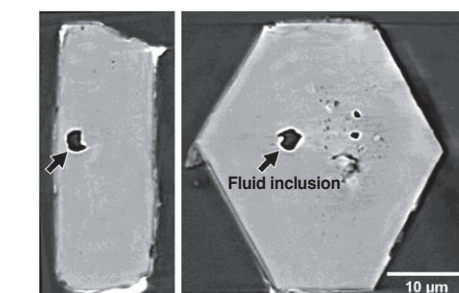


Fig. 2 CT image of carbonated liquid water that fills hole in hexagonal tabular crystal (iron sulfide)

3D Observation of Magnetization Reversal Behavior in Advanced Permanent Magnet

High-performance permanent magnets are indispensable materials for environmental and energy-saving technologies. They are commonly used in motors for electric vehicles, air conditioners, and wind power generators. However, their magnet performance needs to be further improved to increase the energy efficiency of their applications. The key is coercivity, which is one of the crucial parameters that determine the performance of magnetic materials. The magnetization of permanent magnets with high coercivity is difficult to reverse, maintaining their magnetic force even under strong magnetic fields and at high temperatures. The widely used neodymium magnet is a sintered material consisting of Nd-Fe-B magnetic particles with a diameter of a few microns. Therefore, observing the magnetization reversal behavior of individual particles constituting a magnet will elucidate the microscopic mechanism of emerging high coercivity, leading to the development of high-performance magnets. However, conventional magnetic imaging techniques can only be applied to observe the sample surface but not the magnetic domains inside the bulk magnet.

The three-dimensional (3D) observation of magnetic domain structures inside a bulk magnet has become possible using the hard X-ray magnetic tomography technique recently developed at BL39XU of SPring-8. This technique combines scanning magnetic imaging using a circularly polarized hard X-ray microbeam with a tomography method. It has been applied to a fine-grained Nd-Fe-B sintered magnet, an advanced high-performance permanent magnet (Fig. 1). Fig. 2(a) shows images of the 3D microstructure and the magnetic domain structure of the sample in the same observation area. The high-resolution microstructure image was obtained by combining X-ray tomography and 3D scanning electron microscopy (3D-SEM), whereas the magnetic domain image was obtained by X-ray magnetic tomography. In Fig. 2(b), the microscopic magnetization reversal behavior was visualized in 3D by observing the internal magnetic domain structure changing along the magnetic hysteresis curve. The nucleation sites of magnetic domain formation were identified by examining the relationship between the magnetic domain evolution and the microstructure in detail. The results will provide helpful information for elucidating the coercivity mechanism.

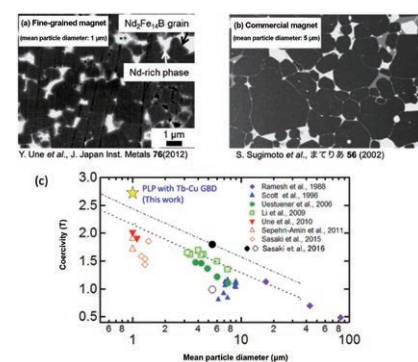


Fig. 1 Microstructures of (a) advanced fine-grained and (b) commercial permanent magnets. (c) Increase in coercivity by reduction in particle diameter.

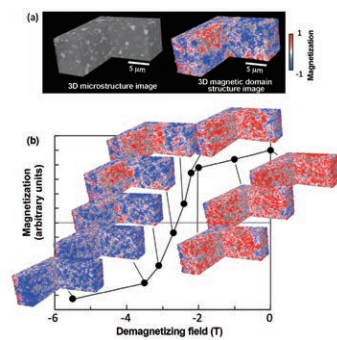


Fig. 2 Hard X-ray magnetic tomography observation of a fine-grained Nd-Fe-B sintered magnet. (a) 3D microstructure image (left) and 3D magnetic domain structure image (right). (b) Changes in the 3D magnetic domain structure of the sample measured while changing magnetic field. The magnetization reversal behavior of individual particles was visualized.

BL39XU Motohiro Suzuki (Kwansei Gakuin University), Satoshi Okamoto (Institute of Multidisciplinary Research for Advanced Materials (IMRAM), Tohoku University) M. Takeuchi, M. Suzuki, S. Kobayashi, Y. Kotani, T. Nakamura, N. Kikuchi, A. Bolyachkin, H. Sepehri-Amin, T. Okubo, K. Hono, Y. Ue, and S. Okamoto, *NPG Asia Mater* 14, 70 (2022).

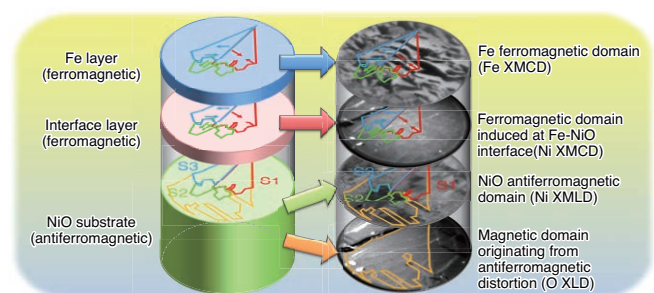
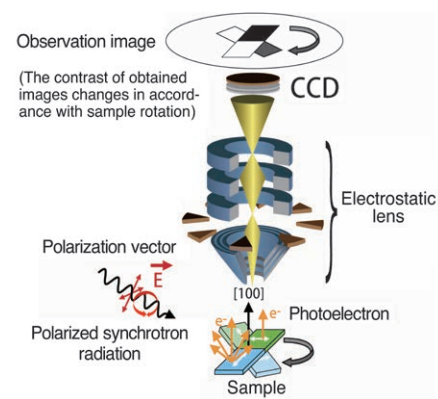
Visualization of magnetic domain structure at the interface of magnetic thin films

In modern society, we receive great benefit from magnetic recording devices such as memories and hard disks. These magnetic recording devices make use of the phenomenon called exchange bias, and its detailed clarification is necessary to use the phenomenon in a wider range of applications. For example, the observation of the exchange coupling of spins between an antiferromagnetic substrate and a ferromagnetic thin film formed on it is required. The element-specific observation of magnetic domains of various magnetic materials is realized by combining photoemission electron microscopy (PEEM), X-ray magnetic circular and linear dichroisms (XMCD & XMLD) using BL17SU and BL25SU. The figure shows the schematic of this experimental method. Depending on the direction of magnetization in the magnetic domain of a sample and the direction of the polarization vector of the incident X-ray, the number of electrons emitted from the surface differs. The image of the region where many electrons are emitted is bright whereas that of the region with fewer electrons being emitted is dark, when the images are magnified using an electrostatic lens.

In this study, an iron (Fe) thin film (thickness, ~0.9 nm) was formed on a nickel oxide (NiO) substrate, which is known as a typical antiferromagnetic material, to analyze the magnetic structure. Using various states of magnetic dichroism at the absorption edges of elements constituting the system, information on (1) the magnetic domain originating from the antiferromagnetic distortion of the NiO substrate (yellow frame), (2) three magnetic domains (S1-S3) originating from spin ordering, (3) the ferromagnetic domain of the top layer of the Fe thin film, and (4) the ferromagnetic domain of the interface (in which Fe, Ni, and O are mixed) is obtained. The sample was rotated with respect to the incident direction of the light. From the change in the contrast of the obtained images, the spin directions in each magnetic domain were determined. The exchange coupling of spins among the substrate, top layer, and interface was clarified.

This observation technique is considered to be applicable to the development of new materials for inductor circuits, in addition to magnetic recording. At SPring-8, this technique is combined with time-resolved measurement of the movements of the magnetic domain and wall with respect to an external field.

BL17SU, BL25SU Toyohiko Kinoshita (JASRI)



(Top) Schematic of magnetic domain observed by PEEM. (Bottom) Results of observation of magnetic domain in antiferromagnetic substrate and in Fe surface and interface of Fe/NiO (100). The arrows indicate the directions of magnetization (spins) in magnetic domains

Simultaneous Production of Hydrogen and Hydrogen Peroxide by Photocatalysis of Red Rust

CO₂-free hydrogen production using solar energy is attracting attention as a technology that can help realize a decarbonized society. The simultaneous production of hydrogen and other useful chemical products by photocatalytic solar water splitting will lead to the development of solar utilization systems with higher added value.

In this study, the surface of hematite, called red rust, was coated with a composite oxide containing tin and titanium using mesocrystal technology, which involves precisely aligning nanoparticles (with dimensions of several tens of nanometers) in photocatalysts to control the flow of electrons and holes. As a result, hydrogen and hydrogen peroxide were generated with very high efficiency and selectivity. When hematite was doped with tin and titanium ions and calcined at 700°C, first tin and then titanium were deposited on the surfaces of the particles. A composite oxide (SnTiO_x) cocatalyst with high selectivity for hydrogen peroxide production was thus formed (Fig. 1). The changes in structure resulting from the doping were clarified by the chemical state analysis of each element by X-ray absorption spectroscopy using high-luminosity synchrotron radiation, by atomic structure analysis via high-resolution total scattering measurements, and by high-resolution electron microscopic analysis using electron energy-loss spectroscopy. When a voltage was applied to a photocatalyst electrode made of hematite doped with tin and titanium ions, the water-splitting reaction proceeded under irradiation with simulated sunlight. The photocurrent density, corresponding to the rate of hydrogen production, and the Faradaic efficiency, indicating the selectivity of hydrogen peroxide, were examined. The results showed that hydrogen and hydrogen peroxide were simultaneously produced with high efficiency and selectivity (Fig. 2a). Also, a first-principles calculation suggested that the SnTiO_x cocatalyst that formed on the hematite was a SnO₂/SnTiO₃ layer with a thickness of a few nanometers (Fig. 2b).

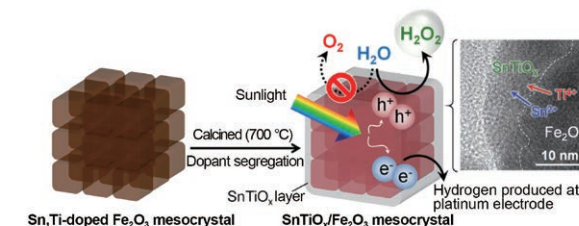


Fig. 1 Mesocrystal photocatalyst for hydrogen and hydrogen peroxide production.

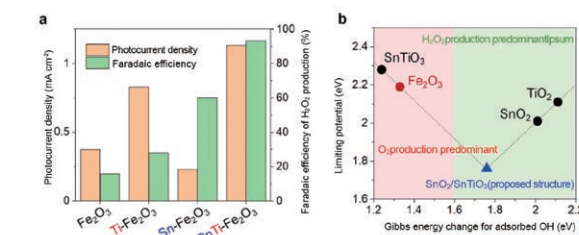


Fig. 2 Photocatalytic water-splitting properties and exploration of highly active cocatalyst.

BL01B1, BL04B2 Takashi Tachikawa (Kobe University) Article: Z. Zhang *et al.*, *Nature Communications* 13, 1499 (2022)

Visualization of magnetic domain structure at the interface of magnetic thin films

In modern society, we receive great benefit from magnetic recording devices such as memories and hard disks. These magnetic recording devices make use of the phenomenon called exchange bias, and its detailed clarification is necessary to use the phenomenon in a wider range of applications. For example, the observation of the exchange coupling of spins between an antiferromagnetic substrate and a ferromagnetic thin film formed on it is required. The element-specific observation of magnetic domains of various magnetic materials is realized by combining photoemission electron microscopy (PEEM), X-ray magnetic circular and linear dichroisms (XMCD & XMLD) using BL17SU and BL25SU. The figure shows the schematic of this experimental method. Depending on the direction of magnetization in the magnetic domain of a sample and the direction of the polarization vector of the incident X-ray, the number of electrons emitted from the surface differs. The image of the region where many electrons are emitted is bright whereas that of the region with fewer electrons being emitted is dark, when the images are magnified using an electrostatic lens.

In this study, an iron (Fe) thin film (thickness, ~0.9 nm) was formed on a nickel oxide (NiO) substrate, which is known as a typical antiferromagnetic material, to analyze the magnetic structure. Using various states of magnetic dichroism at the absorption edges of elements constituting the system, information on (1) the magnetic domain originating from the antiferromagnetic distortion of the NiO substrate (yellow frame), (2) three magnetic domains (S1-S3) originating from spin ordering, (3) the ferromagnetic domain of the top layer of the Fe thin film, and (4) the ferromagnetic domain of the interface (in which Fe, Ni, and O are mixed) is obtained. The sample was rotated with respect to the incident direction of the light. From the change in the contrast of the obtained images, the spin directions in each magnetic domain were determined. The exchange coupling of spins among the substrate, top layer, and interface was clarified.

This observation technique is considered to be applicable to the development of new materials for inductor circuits, in addition to magnetic recording. At SPring-8, this technique is combined with time-resolved measurement of the movements of the magnetic domain and wall with respect to an external field.

BL17SU, BL25SU Toyohiko Kinoshita (JASRI)

Bimetallic Sword Provides Information about Use of Iron during Transition to Iron Age

Bimetallic products consisting of bronze or copper and iron are characteristic archaeological remains in northern Iran from the beginning of Iron Age (about 3,200 years ago). Most of the known bimetallic objects, especially swords, are museum materials without provenance, and little archaeological understanding about them has been obtained. The history of bimet technology might be clear by using the destructive method. However, scientists are reluctant to perform destructive investigations on cultural properties. In this study, we performed the three-dimensional computed tomography (CT) imaging of a bimetallic sword at a resolution of 0.015 mm using 200 keV high-energy X-rays at BL28B2.

Results revealed that a bronze sword with an iron core had modern repairment. On the other hand, the interior CT images of bronze hilts reconstructed using the software developed at SPring-8 were remarkable. Bimetallic swords were produced by inserting an iron sword into a mold with the shape of the hilt and then pouring bronze into the mold. These swords are the world's oldest "insert castings" on bronze and iron. Using this technique, a bronze hilt was cast by fixing a bronze pommel prepared in advance to an iron sword, inserting the sword in a mold, and casting a bronze hilt. The research results show that bimetallic swords are important archaeological remains when discussing the social changes associated with the spread of ironware.



Fig. 1 "Ear pommel sword" considered to be world's oldest example of insert casting.

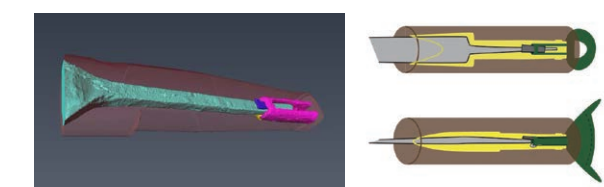


Fig. 2 3D reconstructed image of interior of hilt obtained at BL28B2 (top) and schematics of casting process (bottom).

BL28B2 Ryuji Shikaku (Chief Curator) (Okayama Orient Museum)

Mechanism of Adhesion between High-Performance Fluororesin Coating and Metal Substrate Clarified at Atomic Level

Fluororesin has excellent heat resistance and chemical resistance. Cooking utensils such as metal frying pans and the inner pots of rice cookers are often coated with fluororesin. On the other hand, the adhesion between fluororesin and metals has not been sufficient for fluororesin coatings to be used in medical equipment and automobiles, where high reliability is required, which has been an obstacle to the widespread adoption of fluororesin in those areas. To commercialize fluororesin in areas where high reliability is required, it is necessary to clarify the adhesion mechanism and demonstrate the reliability of products.

Chemical state analysis by X-ray photoelectron spectroscopy (XPS) is effective for revealing the chemical state of the interface between the resin and a metal, the key factor for understanding the adhesion mechanism. However, only depths of up to a few nanometers from the surface can be analyzed by conventional equipment in a laboratory. Although depths of up to ~20 nm can be analyzed by hard X-ray photoelectron spectroscopy (HAXPES*) at SPring-8, the analysis of the interface between the resin and a metal in actual products has been impossible because the interface is located at a depth of 10 μm or more from the surface.

In this study, an original sample fabrication technique was developed to reduce the thickness of a metal layer to 20 nm or less. With this technique, we fully demonstrated the ability of HAXPES to accurately analyze the chemical state of the interface between a resin and a metal (Fig. 1). In addition to performing HAXPES using BL16XU and BL46XU, we used multiple analytical techniques, including transmission electron microscopy, to perform a comprehensive analysis. As a result, it was revealed for the first time that high adhesion is due to the formation of new carbon-oxygen-metal bonds between fluororesin and the metal produced by electron beam irradiation (Fig. 2). As a result of this breakthrough, we gained credibility with our customers by disclosing the mechanism of adhesion as well as the characteristic values for high adhesion, contributing to the increased use of fluororesin coatings (product name: cross-linked fluororesin FEX®). *HAXPES: hard X-ray photoelectron spectroscopy

BL16XU, BL46XU Yugo Kubo (Sumitomo Electric Industries, Ltd.)
 Article: Yugo Kubo *et al.*, *ACS Applied Materials & Interfaces* **10**, 44589 (2018)
 Yugo Kubo *et al.*, *ACS Applied Nano Materials* **5**, 6757 (2022)

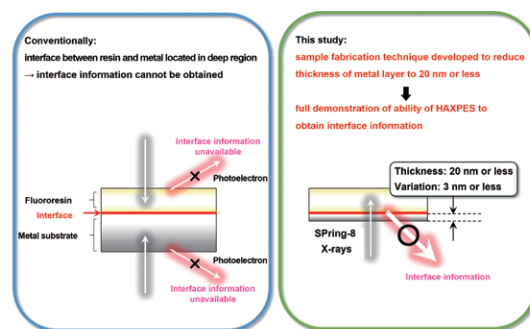


Fig. 1 Chemical state analysis of interface between resin and metal by HAXPES.

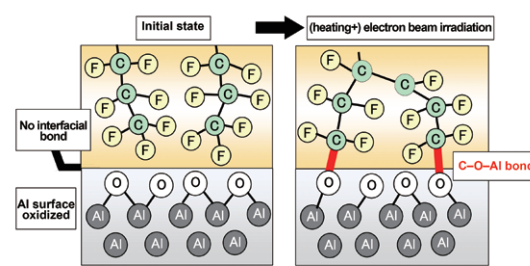


Fig. 2 Mechanism of high adhesion between fluororesin and metal (C: carbon; O: oxygen; F: fluorine; Al: aluminum).

Visualization of Micro-Water Generated in Polymer Electrolyte Fuel Cell Supporting Development of New-Generation Toyota Mirai Hydrogen-Powered Car

Hydrogen is a promising energy source for realizing a sustainable society. The spread of fuel cell electric vehicles as “ultimate eco-cars” is expected because they use hydrogen as fuel and emit only water. The performance of polymer electrolyte fuel cells (PEFCs) is affected not only by the properties of materials such as catalysts and electrolytes but also by the drainage efficiency of water produced by power generation. It is thus necessary to understand the behavior of water inside PEFCs.

The information needed for the design of PEFCs includes the micro-level distribution of water inside the PEFCs and its second-order changes. We developed a small evaluation bench for simulating the operation of a fuel cell electric vehicle, a special power-generating tool that transmits X-rays, and a high-speed and high-sensitivity X-ray camera system at the Toyota beamline (BL33XU). Using these devices, we developed an X-ray radiography technique that can “visualize” the water inside PEFCs (Fig. 1).

These measurement techniques are used for the design of channels and materials of PEFCs. A partially narrowed flow channel newly developed by Toyota Motor Corporation supplies air from the channel to the gas diffusion layer, which reduces the oxygen transport resistance and improves the performance. However, the effects of supplied air on water drainage are not yet fully understood. The water distribution in a conventional channel (Fig. 2, left) and that in the partially narrowed flow channel (Fig. 2, right) were compared at SPring-8. In the partially narrowed flow channel, the air supplied to the gas diffusion layer pushed the accumulated water forward and accelerated water drainage, resulting in improved power generation performance even in the presence of water. These technologies developed at SPring-8 were used in the design of the channel separator and gas diffusion layer of the PEFC in the new-generation Mirai hydrogen-powered car launched by Toyota Motor Corporation in December 2020, contributing to its improved performance and reduced cost.

BL33XU Toyota Central R&D Labs., Inc., SOKEN, Inc., and Toyota Motor Corporation

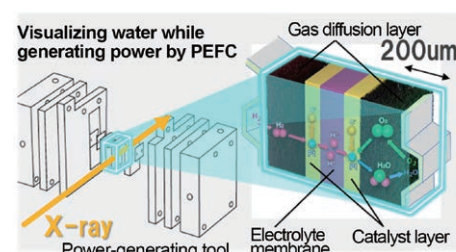


Fig. 1 Schematics of visualization of micro-level water behavior in PEFC by synchrotron radiation X-ray radiography.

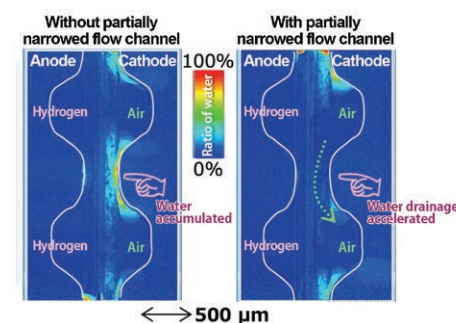


Fig. 2 Observed water distribution. “Without partially narrowed flow channel” and “with partially narrowed flow channel” denote the conventional channel and the newly developed channel adopted in the new-generation Mirai car, respectively.

World’s First Photoelectron Spectroscopy under Atmospheric Pressure and Tracking of Sulfur Poisoning Process of Fuel Cells

Fuel cells are a promising next-generation energy source and are expected to be widely used in automobiles. However, the performance and durability of the electrode catalyst made of the precious metal platinum must be improved to accelerate the implementation of fuel cells. We therefore investigated and clarified the mechanism of the sulfur poisoning process of polymer electrolyte fuel cells, which reduces their lifetime, using photoelectron spectroscopy under atmospheric pressure. Although photoelectron spectroscopy is generally performed under vacuum conditions, we developed a method of photoelectron spectroscopy that can be performed under atmospheric pressure.

X-ray photoelectron spectroscopy (XPS) is an analytical technique used to reveal the chemical state of target elements. The kinetic energy of photoelectrons emitted when a sample is irradiated with X-rays is accurately measured using the apparatus shown in Fig. 1(a). The chemical state is determined on the basis of the electron binding energy obtained by this method. Soft X-rays are usually used as the light source for XPS in a laboratory. However, the use of hard X-rays allows us to observe more deeply inside a substance or to investigate the chemical state of a sample in a gaseous atmosphere. Figure 1(b) shows the photoelectron spectra observed under atmospheric pressure (10⁵ Pa) for the first time in the world, which was realized using the high-luminosity hard X-ray microbeam from the undulator insertion light source at SPring-8.

Figure 2(a) shows the photoelectron spectra of sulfur near the cathode of a polymer electrolyte fuel cell during operation. Not only the identification of existing chemical species but also the determination of the electrical potential of each chemical species is possible by the analysis of fuel cells by photoelectron spectroscopy. It is therefore easy to determine in which of the three phases, i.e., cathode, anode, and electrolyte phases, each chemical species is present. In our experiment, S²⁻ is sulfur that is adsorbed on the platinum electrode and poisons the electrode. The S²⁻ on the cathode oxidized to SO₃²⁻ and dissolves in the electrolyte as the voltage increases, whereas the S²⁻ on the anode remains as S²⁻ on the electrode. In addition, poisoning by S²⁻ is drastically reduced by the use of a platinum-cobalt electrode, demonstrating the effectiveness of such an electrode.

BL36XU Toshihiko Yokoyama (Institute for Molecular Science)
 Article: Y. Takagi *et al.*, *Appl. Phys. Express* **10**, 076603 (2017).

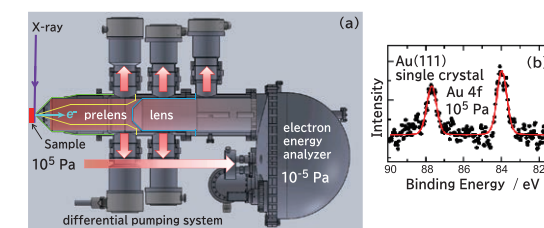


Fig. 1 (a) Schematic diagram of apparatus for hard XPS under atmospheric pressure. (b) Au4f photoelectron spectra of Au(111) single crystal observed under atmospheric pressure for the first time in the world.

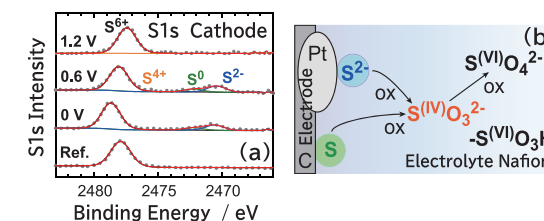


Fig. 2 (a) S1s photoelectron spectra of sulfur from cathode of polymer electrolyte fuel cell during operation. The chemical species of sulfur present depends on the voltage between the cathode and anode. (b) Schematics of chemical species of sulfur adsorbed on and desorbed from the electrode.

Success in visualization of localizations of proteins and lipids in hair

Around the age of 35 years, people’s hair concerns shift from hair damage to hair aging. Curliness, waviness, and dryness are included in the top common hair problems and cause people to feel a change in their hair quality. A well-known change in hair caused by aging is the increase in the number of curly hairs. The localization of proteins in such curly hair has been studied by various methods. However, the localization of lipids in the hair has remained unclear. In this study, the localizations of proteins and lipids were visualized using an infrared (IR) microspectroscopy system at SPring-8. This system combines a microscope and an IR spectrophotometer and can be used to determine the localization of components in a specific region. Information on fine regions has been difficult to obtain with general IR measurement systems. Detailed data on the cross-sectional localization of components in hair have not been available.

Cross-sectional imaging revealed that proteins (amide bonds) and lipids (CH bonds) were uniformly localized in hair with a nearly round cross section and that the inside of the hair had a uniform composition localization (Fig. 1). For curly hair, however, lipids were sparsely localized (the number of CH bonds was small) at sites where proteins were densely localized (the number of amide bonds was large). In contrast, the lipids were densely localized at sites where proteins were sparsely localized (Fig. 2). That is, the localizations of proteins and lipids were in an inverse relationship.

In this study, an uneven localization of hair components, such as proteins and lipids, in curly hair was confirmed at the microlevel by visualizing a more detailed localization of hair components than before. It was found that the localization of proteins is different from that of lipids in curly hair; this is the so-called state of “hair distortion”. Therefore, the curliness of hair can be improved by correcting the uneven localizations of proteins and lipids throughout the curly hair.

BL43IR Satoshi Inamasu (Kracie Home Products, Ltd.)

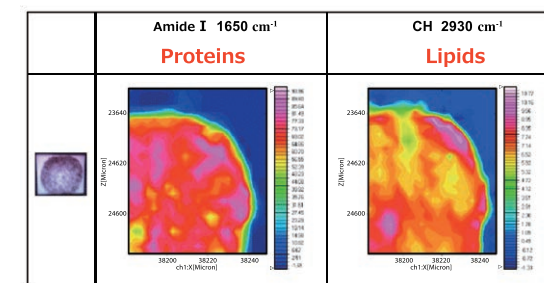


Fig. 1 Mapping of components in hair with a nearly round cross section Red region has a dense localization of components

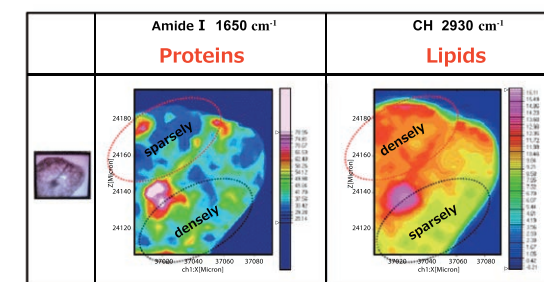
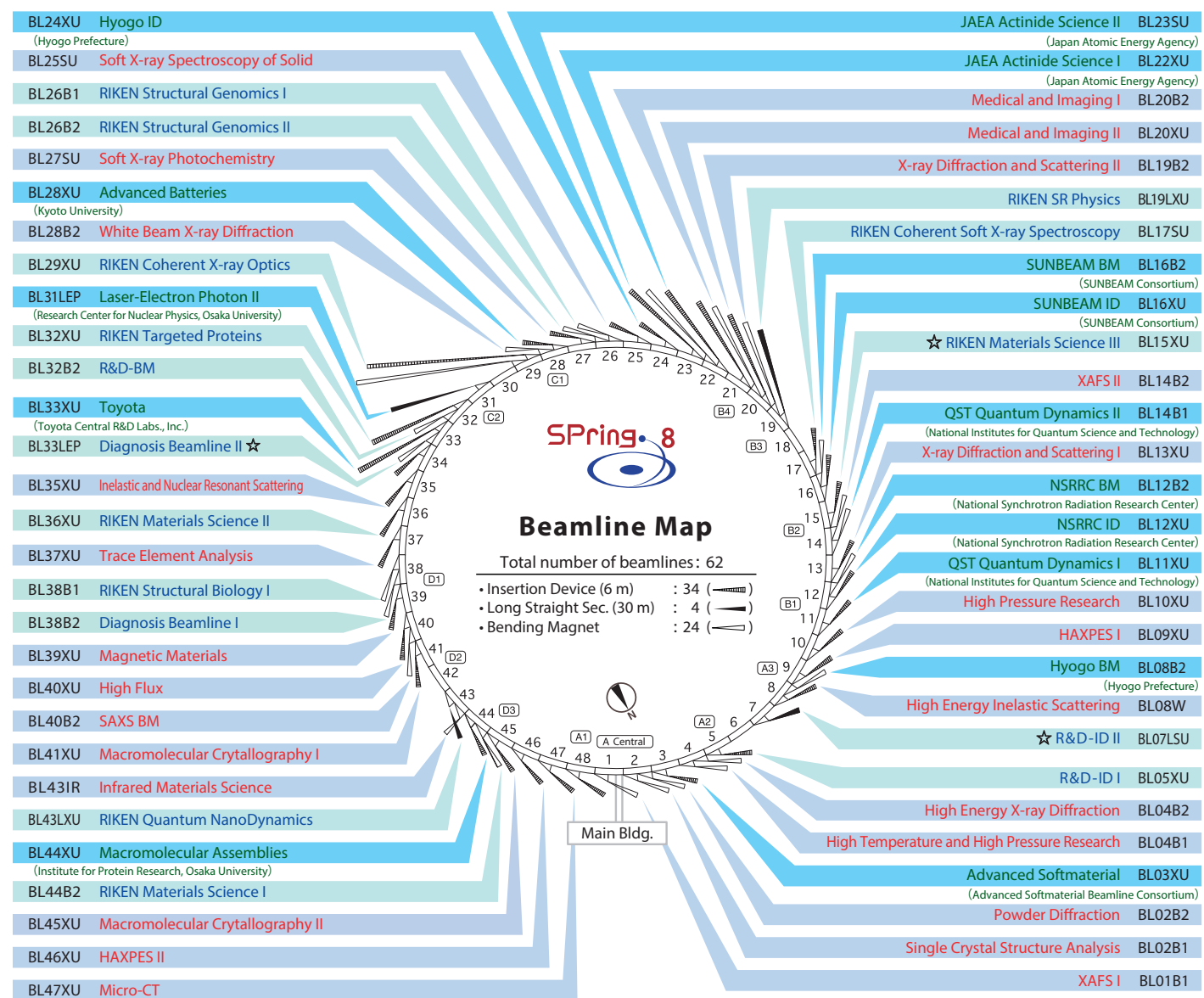


Fig. 2 Mapping of components in curly hair

SPring-8 Beamline

● Beamline Map

The beamlines are shown below with the names, source types and locations. The lengths of normal beamlines are designed to be less than 80 m from the source point.
The lengths of nine and three beamlines are able to extend to 300 m and 1,000 m, respectively.



Apr, 2023

BL : Beamline
B1, B2 : Bending Magnets
XU : X-ray Undulator
SU : Soft X-ray Undulator
W : Wiggler
IR : Infrared Radiation
LEP : Laser-Electron Photon
LXU : Long-length X-ray Undulator
LSU : Long-length Soft X-ray Undulator

Public Beamlines (light blue)
Contract Beamlines (dark blue)
RIKEN Beamlines (green)
★ Planned or Under Construction

- Public Beamlines constructed by SPring-8 and opened for users in Japan and from overseas.
- Contract Beamlines constructed by external organizations for their exclusive use.
- RIKEN Beamlines constructed by RIKEN for its own research.

● Tables of Beamlines in Use

Light source types and photon energies are designed according to each beamline's research requirements.
Basic research equipment is installed in the experimental station.

SPring-8 Beamlines

	Public	Contract	RIKEN	Total
Operational	26	15	13	54
Under Construction	0	0	3	3
Total	26	15	16	57

Public Beamlines (26)

Name of Beamline	Beamline No.	Source	Photon Energy
XAFS I	BL01B1	BM	3.8 ~ 113 keV
Single Crystal Structure Analysis	BL02B1	BM	5 ~ 115 keV
Powder Diffraction	BL02B2	BM	12 ~ 37 keV
High Temperature and High Pressure Research	BL04B1	BM	20 ~ 150 keV
High Energy X-ray Diffraction	BL04B2	BM	37.8 ~ 113.4 keV
High Energy Inelastic Scattering	BL08W	W	110 ~ 300 keV
HAXPES I	BL09XU	U	4.91 ~ 12 keV
High Pressure Research	BL10XU	U	6 ~ 61 keV
X-ray Diffraction and Scattering I	BL13XU	U	5 ~ 72 keV
XAFS II	BL14B2	BM	3.8 ~ 72 keV
X-ray Diffraction and Scattering II	BL19B2	BM	5 ~ 72 keV
Medical and Imaging II	BL20XU	U	7.62 ~ 61 keV
Medical and Imaging I	BL20B2	BM	5.0 ~ 113.3 keV
Soft X-ray Spectroscopy of Solid	BL25SU	U	0.12 ~ 2 keV
Soft X-ray Photochemistry	BL27SU	U	0.17 ~ 3.3 keV
White Beam X-ray Diffraction	BL28B2	BM	5 ~ 200 keV
Inelastic and Nuclear Resonant Scattering	BL35XU	U	14.4 ~ 100 keV
Trace Element Analysis	BL37XU	U	4.5 ~ 113 keV
Magnetic Materials	BL39XU	U	5 ~ 37 keV
High Flux	BL40XU	U	8 ~ 17 keV
SAXS BM	BL40B2	BM	6.5 ~ 22 keV
Macromolecular Crystallography I	BL41XU	U	6.5 ~ 35 keV
Infrared Materials Science	BL43IR	BM	10 meV ~ 2 eV
Macromolecular Crystallography II	BL45XU	U	6.5 ~ 16 keV
HAXPES II	BL46XU	U	6 ~ 37 keV
Micro-CT	BL47XU	U	5.2 ~ 37.7 keV

Contract Beamlines (15)

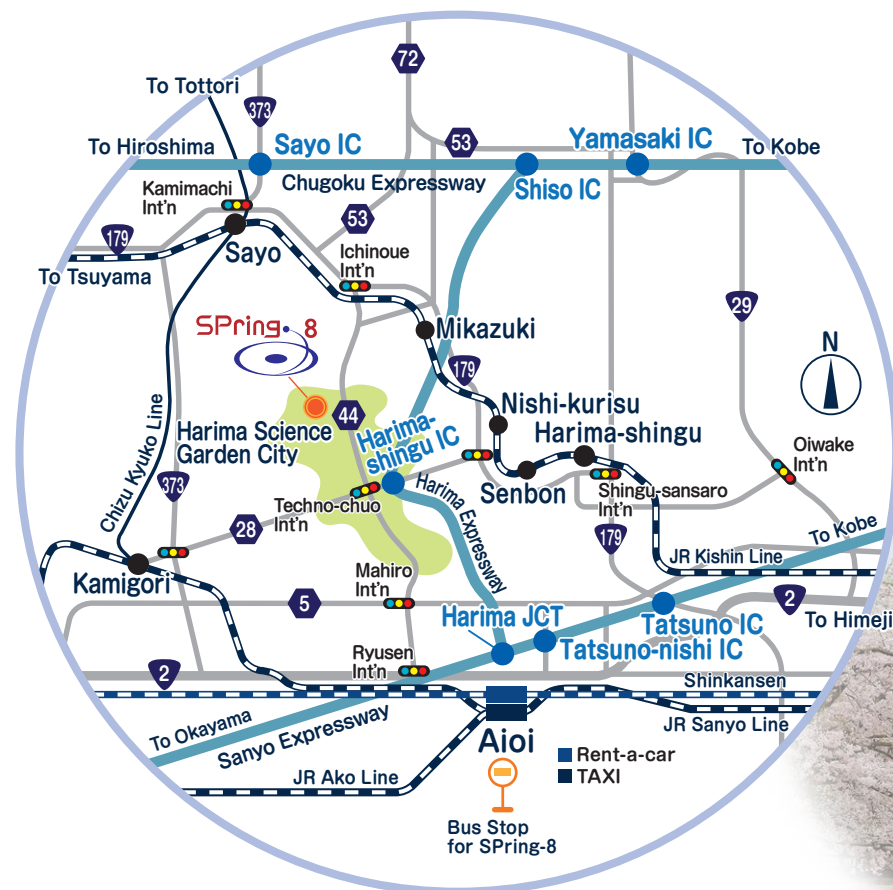
Name of Beamline	Beamline No.	Source	Photon Energy
Advanced Softmaterial (Advanced Softmaterial Beamline Consortium)	BL03XU	U	6 ~ 35 keV
Hyogo BM (Hyogo Prefecture)	BL08B2	BM	4.6 ~ 20 keV
Hyogo ID (Hyogo Prefecture)	BL24XU	U	5 ~ 20 keV
NSRRC ID (National Synchrotron Radiation Research Center)	BL12XU	U	4.5 ~ 30 keV
NSRRC BM (National Synchrotron Radiation Research Center)	BL12B2	BM	7 ~ 35 keV
SUNBEAM ID (SUNBEAM Consortium)	BL16XU	U	4.5 ~ 40 keV
SUNBEAM BM (SUNBEAM Consortium)	BL16B2	BM	4.5 ~ 113 keV
Advanced Batteries (Kyoto University)	BL28XU	U	4 ~ 46 keV
Toyota (Toyota Central R&D Labs., Inc.)	BL33XU	U	4 ~ 72 keV
Laser-Electron Photon II (Research Center for Nuclear Physics, Osaka University)	BL31LEP	LEP	1.4 ~ 2.9 GeV
Macromolecular Assemblies (Institute for Protein Research, Osaka University)	BL44XU	U	6.5 ~ 17.7 keV
QST Quantum Dynamics I (National Institutes for Quantum Science and Technology)	BL11XU	U	6 ~ 70 keV
QST Quantum Dynamics II (National Institutes for Quantum Science and Technology)	BL14B1	BM	5 ~ 150 keV
JAEA Actinide Science I (Japan Atomic Energy Agency)	BL22XU	U	4 ~ 70 keV
JAEA Actinide Science II (Japan Atomic Energy Agency)	BL23SU	U	0.4 ~ 1.8 keV

RIKEN Beamlines (16)

Name of Beamline	Beamline No.	Source	Photon Energy
RIKEN Materials Science III	BL15XU	U	
RIKEN Coherent Soft X-ray Spectroscopy	BL17SU	U	0.225 ~ 2.0 keV
RIKEN SR Physics	BL19LXU	U	7.1 ~ 51 keV
RIKEN Structural Genomics I	BL26B1	BM	6 ~ 17 keV
RIKEN Structural Genomics II	BL26B2	BM	6 ~ 17 keV
RIKEN Coherent X-ray Optics	BL29XU	U	4.4 ~ 56 keV
RIKEN Targeted Proteins	BL32XU	U	9 ~ 18 keV
RIKEN Materials Science II	BL36XU	U	4.5 ~ 35 keV
RIKEN Structural Biology I	BL38B1	BM	6.5 ~ 14 keV
RIKEN Quantum NanoDynamics	BL43LXU	U	14.4 ~ 25 keV
RIKEN Materials Science I	BL44B2	BM	15.5 ~ 30.2 keV
R&D-ID I	BL05XU	U	7 ~ 15 keV
R&D-ID II	BL07LSU	U	0.25 ~ 2 keV
R&D-BM	BL32B2	BM	
Diagnosis Beamline II	BL33LEP	LEP	1.5 ~ 2.9 GeV
Diagnosis Beamline I	BL38B2	BM	

Location of SPring-8

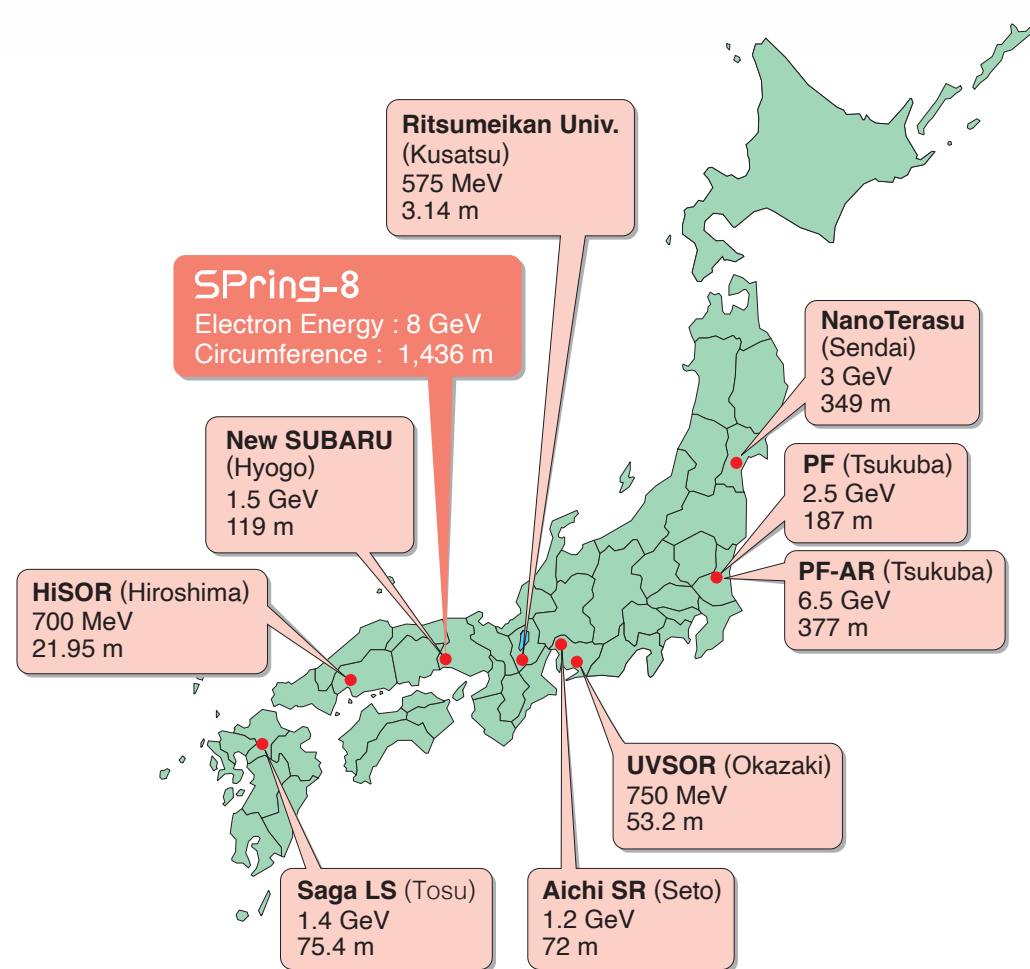
SPring-8 is located at the north end of the Harima Science Garden City, which is a part of the Nishiharima Technopolis. The Hyogo Prefectural Government is actively promoting the area as an attractive location for activities related to science and technology.



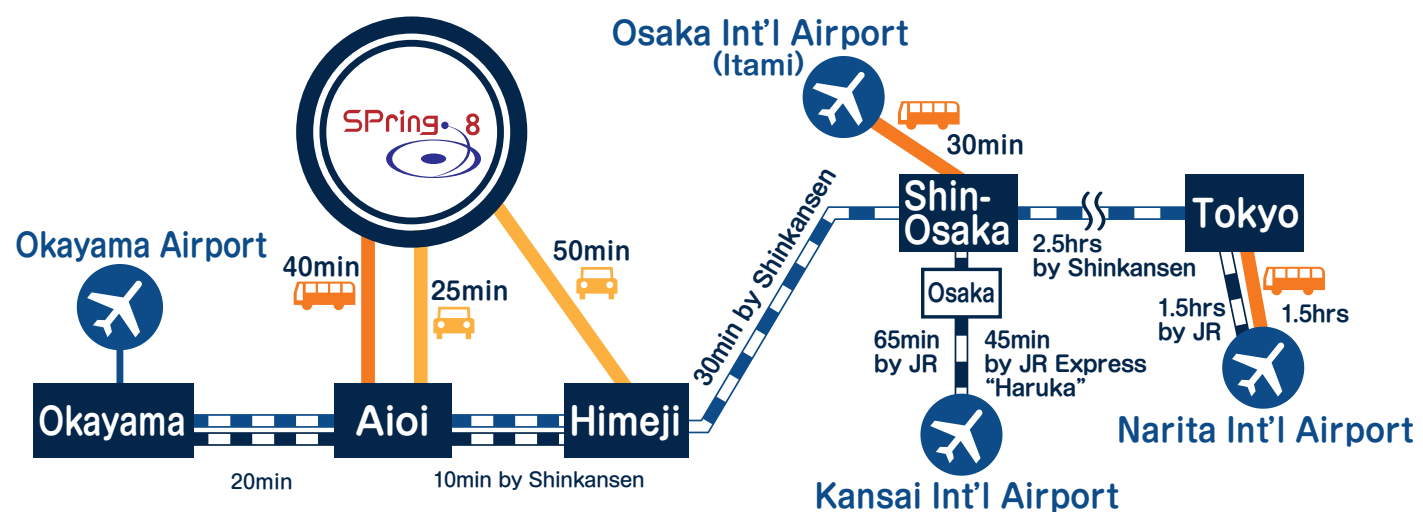
Himeji Castle, also called Shirasagi-jo (White Heron Castle) due to its white outer walls, is located in the center of Himeji City, about 50 kilometers east of SPring-8. It is the best preserved castle in all of Japan, registered on UNESCO's World Heritage list in 1993.



Synchrotron Radiation Facilities for Public Use in Japan



Access to SPring-8



SR Facilities around the World

